Department of Chemistry
Faculty of Science
University of Helsinki

Probing gas-phase radical reactions and modeling the detection of aerosol precursors using computational and experimental methods

Siddharth Iyer

Academic Dissertation

To be presented, with the permission of the Faculty of Science of the University of Helsinki, for public examination in Auditorium D101, Physicum, Gustaf Hällströmin katu 2, 00560, Helsinki, on October 4th, 2019, at 12 noon.

Helsinki 2019

University of Helsinki
Finland

Supervisors

Theo Kurtén, University of Helsinki, Finland and Matti P. Rissanen, Tampere University, Finland

Pre-examiners

David R. Hanson, Augsburg College, Minneapolis, United States
Kari Laasonen, Aalto University, Finland

Opponent

David Glowacki, University of Bristol, United Kingdom

Supervising professor and custos

Lauri Halonen, University of Helsinki, Finland

Contact information

Siddharth Iyer
Department of Chemistry
P.O. Box 55
FI-00014 University of Helsinki
siddharth.iyer@helsinki.fi

ISBN 978-951-51-5500-9 (paperback)
ISBN 978-951-51-5501-6 (PDF)
http://ethesis.helsinki.fi/

Unigrafia
Helsinki 2019

Abstract

Understanding the gas-phase chemistry of secondary organic aerosol (SOA) formation is critical for accurate estimation of the effect of these aerosol on Earth's radiative balance. Additionally, the direct detection of the precursor molecules involved in these chemical reactions at atmospheric pressure without pre-treatment is valuable. In this work, computational and experimental methods are employed to 1) elucidate the thermodynamics and the mechanisms of selected key radical-radical reactions in the atmosphere and 2) investigate the efficiency of some of the chemical ionization mass spectrometry methods in detecting the atmospherically relevant acids and precursor compounds involved in the formation of SOA.

The main oxygen containing radical species in our atmosphere, and also the key focus of this study, are hydroxy (OH), hydroperoxy (HO_2), alkoxy (RO) and peroxy (RO_2) radicals. Our computational study on the favorability of the radical recycling product channels of RO_2 + HO_2 and RO_2 + RO_2 reactions (RO + OH + O_2 and RO + RO + O_2, respectively) for RO_2s derived from the oxidation of a set of the highest globally emitted monoterpenes showed that the two reactions were thermodynamically favorable for all the studied systems, and that for some of them, especially the O_3 oxidized systems, the rate-limiting transition state energies can be low enough to render the reactions competitive in atmospheric conditions. Peroxy radical reactions with the atmospheric oxidant OH and alkoxy radicals RO were found to first form a trioxide adduct (ROOOH and ROOOR, respectively). While the former rapidly decompose to RO + HO_2 and R(O)OH + O_2 products for the model β-oxo and acetyl RO_2 systems, respectively, the ROOOR adducts from the latter can have lifetimes in the range of 10 - 100 s (for the homo and hetero alkyl and β-oxo systems). We note that the concentrations of these adducts are quite small (3×10^4 molecules cm^{-3} at the higher limit of ambient RO concentrations). However, if the reacting RO_2 and RO radicals are sufficiently large and oxidized, the product adducts can directly be involved in SOA formation.

The modeling of iodide-based chemical ionization mass spectrometer (iodide-CIMS) using computational methods showed that relatively low-level computational theory can produce reasonable correlation between molecule·I^- cluster binding enthalpies and iodide-CIMS instrumental sensitivities . While some outliers were observed (lower than expected binding enthalpies for clusters that were detected at the maximum possible sensitivity of the instrument, for example), the method outlined in our study can be a quick indicator of the detectibility of an analyte by an iodide-CIMS. Additionally, the direct detection of the HO_2 radical experimentally using an iodide-CIMS was demonstrated. The comparison of iodide- and nitrate-CIMS spectra for a cyclohexene ozonolysis experiment showed that the iodide-CIMS method was capable of detecting the less oxidized (oxygen:carbon O/C ratio of 0.5 - 0.66) molecules more efficiently than nitrate-CIMS. Higher oxidized molecules (O/C ratio 1 - 1.5) were detected equally well by both methods. Finally, the use of a new chemical ionization inlet (Multi-scheme chemical IONization inlet, MION, Karsa Ltd, Helsinki, Finland), which is capable of switching between two different reagent ions, bromide and nitrate, in 1 s timescales was demonstrated and used to detect the ozonolysis products of cyclohexene and α-pinene. Similarly to iodide-CIMS, the bromide-CIMS was more adept at detecting the less oxidized species than the nitrate-CIMS, whereas the higher oxidized molecules were more efficiently detected by the nitrate-CIMS method. The successful demonstration of the MION inlet opens up the possibility to use multiple CIMS methods concurrently and detect a widest possible range of volatile organic compound (VOC) oxidation products.

Acknowledgements

I would like to thank all those who made the research presented in this thesis possible: my supervisors Theo Kurtén and Matti Rissanen, Academy of Finland for the funding and CSC-IT Center for Science for the computing resources. I also thank Prof. Lauri Halonen for giving me the opportunity to work in the department of molecular science and for his lectures that have taught me so much. I am very grateful to Assistant Professor David R. Hanson and Professor Kari Laasonen for reviewing my thesis, and all of my co-authors for their detailed comments on my articles.

At the start of my PhD work, while I was only still learning the ropes, I was lucky to have my early results turn into multiple co-authored articles written by Joel Thornton's group in the University of Washington. Two names in particular in addition to Joel that I would like to mention are Ben Lee and Felipe Lopez-Hilifiker. I am grateful to them for giving me the valuable boost at the start of my PhD journey.

I had just the one colleague when I started my work, Noora, and I am grateful for having someone as resourceful as her teach me the ropes at such a critical time. I would also like to thank the rest of my colleagues in the office, Galib, Kajsa, Matthieu, Niko, Rashid, Thomas and Vili, and my colleague and co-author from the Physics side, Lance. You guys made work days both interesting and fun. I would also like to thank the Simu group members for the educative joint group meetings and for the informal non-work related events.

I was extremely lucky in my PhD endeavor to be mentored by two supervisors, Theo Kurtén and Matti Rissanen, who mentored me in theoretical calculations and in experimental mass spectrometry work, respectively. I have learned immensely both from their comments on my early manuscripts, and through our discussions. That learning will stick with me throughout my academic career.

Finally, I would like to thank my parents and my brother for their constant support despite the distance. It was not easy to be so far away from those I love the most, but you always made me feel that you were right beside me cheering me on.

Siddharth Iyer
Helsinki, 2019

List of Publications

List of publications included in the thesis:

I. **Siddharth Iyer**, Felipe Lopez-Hilfiker, Ben H. Lee, Joel A. Thornton, Theo Kurtén. Modeling the detection of organic and inorganic compounds using iodide-based chemical ionization. *The Journal of Physical Chemistry A* **2016**, *120*, 576-587.

II. **Siddharth Iyer**, Xucheng He, Noora Hyttinen, Theo Kurtén, Matti P. Rissanen. Computational and experimental investigation of the detection of HO_2 radical and the products of its reaction with cyclohexene ozonolysis derived RO_2 radicals by an iodide-based chemical ionization mass spectrometer. *The Journal of Physical Chemistry A* **2017**, *121*, 6778-6789.

III. **Siddharth Iyer**, Heidi Reiman, Kristian H. Møller, Matti P. Rissanen, Henrik G. Kjaergaard, Theo Kurtén. Computational investigation of $RO_2 + HO_2$ and $RO_2 + RO_2$ reactions of monoterpene derived first-generation peroxy radicals leading to radical recycling. *The Journal of Physical Chemistry A* **2018**, *122*, 9542-9552.

IV. **Siddharth Iyer**, Matti P. Rissanen, Theo Kurtén. Reaction between peroxy and alkoxy radicals can form stable adducts. *The Journal of Physical Chemistry Letters* **2019**, *10*, 2051-2057.

V. Matti P. Rissanen, Jyri Mikkilä, **Siddharth Iyer**, Jani Hakala. Multi-scheme chemical ionization inlet (MION) for fast switching of reagent ion chemistry in atmospheric pressure chemical ionization mass spectrometry (CIMS) applications. Atmospheric Measurement Techniques Discussion 2019. https://doi.org/10.5194/amt-2019-159.

The author performed all the calculations of Articles I and IV, a majority of the calculations in Articles II and III, and a significant portion of the laboratory experiment and subsequent data

analysis in Articles II and V. The author wrote the manuscripts for Articles I, II, III and IV.

List of other publications not included in the thesis:

VI. Ahonen, L.; Li, C.; Kubecka, J.; **Iyer, S.**; Vehkamäki, H.; Petäjä, T.; Kulmala, M.; Hogan, C. J. Ion mobility-mass spectrometry of iodine pentoxide-iodic acid hybrid cluster anions in dry and humidified atmospheres. *Journal of Physical Chemistry Letters* **2019**, *10*, 1935-1941.

VII. Lee, B. H.; Lopez-Hilifiker, F. D.; Veres, P. R.; McDuffie, E. E.; Fibiger, D. L.; Sparks, T. L.; Ebben, C. J.; Green, J. R.; Schroder, J. C.; Campuzano-Jost, P.; **Iyer, S.**; D'Ambro, E. L.; et al. Flight deployment of a high-resolution time-of-flight chemical ionization mass spectrometer: observations of reactive halogen and nitrogen oxide species. *Journal of Geophysical Research: Atmospheres* **2018**, *123*, 7670-7686.

VIII. Hyttinen, N.; Otkjaer, R. V.; **Iyer, S.**; Kjaergaard, H. G.; Rissanen, M. P.; Wennberg, P. O.; Kurtén, T. Computational comparison of different reagent ions in the chemical ionization of oxidized multifunctional compounds. *Journal of Physical Chemistry A* **2018**, *122*, 269-279.

IX. Bianchi, F.; Garmash, O.; He, X.; Yan, C.; **Iyer, S.**; Rosendahl, I.; Xu, Z.; Rissanen, M. P.; Riva, M.; Taipale, R.; Sarnela, N.; Petäjä, T.; Worsnop, D. R.; Kulmala, M.; Ehn, M.; Junninen, H. The role of highly oxygenated molecules (HOMs) in determining the composition of ambient ions in the boreal forest. *Atmospheric Chemistry and Physics* **2017**, *17*, 13819-13831.

X. Lopez-Hilifiker, F. D.; **Iyer, S.**; Mohr, C.; Lee, B. H.; D'Ambro, E. L.; Kurtén, T.; Thornton, J. A. Constraining the sensitivity of iodide adduct chemical ionization mass spectrometry to multifunctional organic molecules using the collision limit and thermodynamic stability of iodide ion adducts. *Atmospheric Measurement Techniques* **2016**, *9*, 1505-1512.

XI. Liu, J.; D'Ambro, E. L.; Lee, B. H.; Lopez-Hilifiker, F. D.; Zaveri, R. A.; Rivera-Rios, J. C.; Keutsch, F. N.; **Iyer, S.**; Kurtén, T.; Zhang, Z.; Gold, A.; Surrat, J. D.; Shilling, J. E., Thornton, J. A. Efficient isoprene secondary organic aerosol formation from a non-IEPDX pathway. *Environmental Science and Technology* **2016**, *50*, 9872-9880.

XII. Lee, B. H.; Mohr, C.; Lopez-Hilifiker, F. D.; Lutz, A.; Hallquist, M.; Lee, L.; Romer, P.; Cohen, R. C.; **Iyer, S.**; Kurtén, T.; Hu, W.; Day, D. A.; Campuzano-Jost, P.; Jimenez, J. L.; et al. Highly functionalized organic nitrates in the southeast United States: Contribution to secondary organic aerosol and reactive nitrogen budgets. *Proceedings of the National Academy of Sciences of the United States of America* **2016**, *113*, 1516-1521.

List of Abbreviations

APi	Atmospheric pressure interface
APi-TOF	Atmospheric pressure interface time of flight mass spectrometer
AVOC	Anthropogenic volatile organic compound
BO	Born-Oppenheimer approximation
BVOC	Biogenic volatile organic compound
CI	Criegee intermediate
CI-APi-TOF	Chemical ionization atmospheric pressure interface time of flight mass spectrometer
CIMS	Chemical ionization mass spectrometer
CCN	Cloud condensation nuclei
CC	Coupled cluster
DFT	Density functional theory
DLPNO	Domain based local pair natural orbital
FT-ICR	Fourier transform ion cyclotrone resonance
GDA	Generalized gradient approximation
GTO	Gaussian type orbital
HF	Hartree Fock
HOM	Highly oxygenated organic molecules
IMR	Ion molecule reaction
LDA	Local density approximation
MBPT	Many body perturbation theory
MION	Multi-scheme chemical ionization inlet

POZ	Primary ozonide
PNO	Pair natural orbital
Q	Quadrupole
QIT	Quadrupole ion trap
	RRHO Rigid rotor harmonic oscillator
SOA	Secondary organic aerosol
STO	Slater type orbital
STT	Stratosphere to troposphere transport
TOF	Time-of-flight mass spectrometer
TS	Transition state
TST	Transition state theory
UW-CIMS	University of Washington iodide-based chemical ionization mass spectrometer
VOC	Volatile organic compound

Contents

Abstract **iii**

Acknowledgements **v**

List of Publications **vii**

List of Abbreviations **xi**

1 Introduction **1**
1.1 Objectives of the thesis 3

2 Oxidation of biogenic VOCs and important radical reactions in the atmosphere **5**
2.1 Alkene + Oxidant Reactions 6
2.2 Formation of peroxy and other important radical species in the atmosphere 10

3 Theoretical Background **15**
3.1 Quantum Chemistry 15
3.2 Density functional theory 20
3.3 DFT functionals 20
3.3.1 LDA functionals 21
3.3.2 GGA and meta-GGA functionals 21
3.3.3 Hybrid and double-hybrid functionals 21
3.3.4 Dispersion Corrections 22
3.4 Basis sets 22
3.4.1 Basis set sizes 23
3.5 Cluster thermodynamics and kinetics 24

4 Mass Spectrometry **27**
4.1 Components of a mass spectrometer 27

4.2 Chemical ionization atmospheric pressure interface time of flight mass spectrometer (CIMS) 28
4.2.1 Ionization 30
4.3 Sensitivity of a CIMS instrument 33
4.3.1 Translating binding energies into approximate instrument sensitivities 34

5 Results **39**
5.1 Modeling CIMS sensitivities 39
5.2 Detection of the HO_2 radical 43
5.3 Detection of VOC oxidation products by I^- and Br^- and comparing CIMS methods 44
5.4 Thermodynamics and kinetics of gas-phase peroxy radical reactions 46
5.5 Kinetics of RO_2 + RO reaction on the singlet surface 47

6 Conclusions **51**
6.1 Article I: Cluster binding enthalpies and iodide-CIMS sensitivities 51
6.2 Article II: Theoretical and experimental study of the detection of HO_2 radical and the products of cyclohexene ozonolysis using iodide-CIMS 52
6.3 Article III: Thermodynamics of RO_2 + HO_2 and RO_2 + RO_2 reactions that lead to radical recycling 52
6.4 Article IV: Mechanism to form stable adducts from gas-phase reactions of alkoxy and peroxy radicals 53
6.5 Article V: Rapid switching between reagent ions and the detection of VOC oxidation products 53

References **55**

Introduction

When the Voyager 1 spacecraft took a photo of the Earth from the outer fringes of our solar system, the planet appeared as a faint blue dot, floating against an incomprehensibly vast backdrop of nothingness. A sight that inspired Carl Sagan to coin one of the most famous pieces of writing that resonates with the child-like wonder in all our hearts: "Look again at the dot. That's here. That's home. That's us." That little dot contains all the complexities that can take in sun's light and warmth and transform a watery rock into a cradle for life to thrive. Our atmosphere is crucial in what makes our planet specially suited for life. By attempting to demystify a minute fraction of the complex atmospheric processes, notably some of the crucial elemental reactions that lead to cloud formation, I hope to inspire you to continue to appreciate the planet we call home.

Ambient air is mostly made up of nitrogen (78%) and oxygen (21%). While they are crucial to the planet, other gases in trace concentrations play an equally vital role in making Earth a vibrant, livable planet. The critical role of carbondioxide (CO_2) in allowing plants to convert the light from the sun into food through the process of photosynthesis possibly takes a backseat in most people's minds these days to the disastrous role it plays in global climate change. Other important trace gases include methane and water vapor, both greenhouse gasses that have a net warming effect on the planet. [1, 2, 3, 4] While these molecules are extremely important and are deserving of playing the lead role in a PhD thesis (and this is undoubtedly the case for a number of theses on atmospheric studies), this thesis is not about them. Here, we look at some of the other trace gases, notably those emitted by terrestrial vegetation, that are pivotal in the formation of secondary organic aerosol (SOA).

Here, some introductory text on the importance of SOA and their effect on global climate is warranted. SOA, and most aerosol in general, have a net cooling effect on the planet. This is due principally for two reasons: 1) they

directly reflect sunlight back into space and 2) they lead to the formation of clouds that can subsequently reflect sunlight back into space. The contribution of aerosol is therefore fundamentally in increasing the planet's albedo (or how efficiently the planet can reflect sunlight). Additionally, their crucial role in the formation of clouds directly regulates global climate. While a lot has been learned about the molecular level processes involved in the formation of SOA, one can successfully make the case that we have barely scratched the surface. The role of gas-phase sulfuric acid in the formation of early clusters is now well established. A combination of sulfuric acid and atmospheric base molecules, such as ammonia and some amines, are thought to make up the composition of early clusters. Low-volatile organic molecules are then reported to play a role by condensing on these acid-base clusters and increasing the cluster size to the point where they can act as cloud condensation nuclei (CCN; sizes where water vapor can efficiently condense on them and form clouds).

The process leading to the formation of these low-volatile organic compounds starts with the oxidation of initially highly volatile organic compounds (VOC). While these VOCs can have both anthropogenic (human) and biogenic (natural) sources, this thesis focuses on the biogenically emitted VOCs or BVOCs. One class of BVOCs is monoterpenes, which make up about 11% of the total annual BVOC emission. Monoterpenes are fairly large molecules and their oxidation products make an important part of the lowest-volatility SOA. Molecules belonging to this class have an elemental composition of $C_{10}H_{16}$ and include molecules such as α-pinene, β-pinene, limonene, ocimene, Δ^3-carene, among others. Once emitted, these molecules are rapidly oxidized by the atmospheric oxidants. A detailed account of the oxidation process is provided in Chapter 2. This oxidation process can lead to the formation of highly oxygenated organic molecules (HOM) that can potentially have extremely low volatilities - ideal for condensing onto pre-existing particles and form SOA. [5, 6]

The chemistry underlying these oxidation reactions and the formation of these HOM is broad. In this thesis, we looked at a small subset of these chemical reactions. In addition, the instruments that are currently used to detect the gas-phase precursor molecules involved in the formation of HOM, namely chemical ionization mass spectrometer are not well characterized; the chemistry between the analyte molecules and the reagent ions used in a specific CIMS method are not completely clear. We shed light into this issue specifically for an iodide-based chemical ionization mass spectrometer

(iodide-CIMS) by employing computational methods to characterize the analyte-reagent ion chemistry. In addition, we used multiple CIMS methods in laboratory experiments to detect VOC oxidation products and compared their predilection for molecules with different degrees of oxidation.

1.1 Objectives of the thesis

The main objectives of this thesis are to:

1. Relate calculated molecule·I^- cluster binding enthalpies with their measured iodide-CIMS sensitivities for a set of atmospherically relevant VOC oxidation products and organic and inorganic acids. The iodide-CIMS sensitivities should have a positive correlation to cluster binding enthalpies as fewer of the more strongly bound clusters are likely to lose their charge inside the mass spectrometer relative to the less strongly bound clusters.

2. Predict the instrument sensitivities using the established relation and detect in a laboratory setting presently undetected gas-phase molecules such as the HO_2 radical and the products of cyclohexene oxidation.

3. Explore computationally the thermodynamics and kinetics of gas-phase reactions of peroxy radicals (RO_2) derived from monoterpene oxidation. In particular, study the less explored radical recycling product channels of RO_2 + HO_2 and RO_2 + RO_2. Additionally, investigate the bimolecular reactions of RO_2 with alkoxy radicals and with OH.

Oxidation of biogenic VOCs and important radical reactions in the atmosphere

Terrestrial vegetation is the dominant source of non-methane VOCs in the atmosphere. It accounts for about 90% of the emission total, [7] which is about 1150 Tg C annually. [8] These biogenically derived VOCs (BVOCs) affect both gas-phase and heterogeneous chemistry in the troposphere. [9, 10, 11, 12, 13] These molecules are often quite reactive and their atmospheric lifetimes are therefore correspondingly short, ranging from minutes to hours. [13] They can also have a significant influence on the concentrations of carbon monoxide (CO), OH and ozone. [14, 15, 16] Additionally, they play a critical role in new particle formation in the atmosphere. [17, 18, 19, 20]

The dominant sink channels of the reactive VOCs are reactions with atmospheric oxidants. There are two general mechanisms for the oxidation of alkane and alkene VOCs. Alkane VOC oxidation by OH and NO_3 occurs by H-abstraction from the various C-H bonds. For alkenes, oxidation is more likely from the addition of OH, NO_3 and O_3 to the C=C bond. An illustration of the main sources and sinks of the atmospheric oxidants and the products of some of their reactions with BVOCs is shown in Figure 2.1.

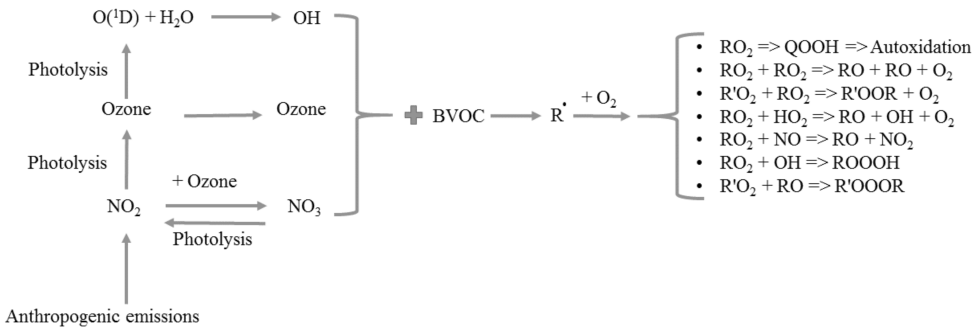

Figure 2.1: A schematic of the main sources of atmospheric oxidants and the products of some of their reactions with BVOCs. Note: anthropogenic emissions only include NO_x here, but should in principle include anthropogenic volatile organic compounds (AVOCs) that are oxidized by OH, NO_3 and O_3.

In the following section, we describe the sources and sinks of these atmospheric oxidants. We limit our description to the oxidation of alkene BVOCs as these were the focus of the articles that comprise this thesis.

2.1 Alkene + Oxidant Reactions

While there are many oxidants in the liquid-phase, the three dominant atmospheric oxidants in the gas-phase are OH, NO_3, and O_3. Daytime OH concentrations in the boundary layer are typically between 1×10^6 and 1×10^7 molecules cm^{-3} in pristine [21] and polluted [22] conditions, respectively. The latter is likely the upper limit of steady state OH concentrations. Despite their relatively low concentrations, OH radicals dominate daytime chemistry in the troposphere due to their high reactivity. For example, the reaction rate coefficients of OH radicals with β-pinene (biogenic VOC) and toluene (anthropogenic VOC) at 298 K are around 9×10^{-11} cm^3 molecule^{-1} s^{-1} [23] and 6×10^{-12} cm^3 molecule^{-1} s^{-1} [24], respectively. The fastest possible bimolecular rates are in the 1×10^{-10} cm^3 molecule^{-1} s^{-1} range due to the gas-kinetic collision limit, so these OH reactions are quite fast.

The dominant OH source in the troposphere is photolysis of ozone and the subsequent reaction of the excited oxygen atom O(^{1}D) with water (see reactions 2.1 and 2.2). Other OH forming channels include the photolysis of nitrous acid (HONO), [25] ozonolysis of alkenes, and photolysis of aldehydes

and peroxides in the presence of NO and NO_2.

$$O_3 \xrightarrow{h\nu} O(^1D) + O_2 \tag{2.1}$$

$$O(^1D) + H_2O \rightarrow 2OH \tag{2.2}$$

The high reactivity of the radical translates to an atmospheric lifetime of OH of less than 1 s. The main OH loss channels in the atmosphere are reactions with CO and CH_4, generating HO_2 and CH_3O_2, respectively.

$$OH + CO \rightarrow CO_2 + H \tag{2.3}$$

$$H + O_2 + M \rightarrow HO_2 + M \tag{2.4}$$

$$OH + CH_4 \rightarrow CH_3 + H_2O \tag{2.5}$$

$$CH_3 + O_2 + M \rightarrow CH_3O_2 + M \tag{2.6}$$

Here M is a third body that only acts to collisionally stabilize the product complex.

OH is a daytime radical since the major OH formation channels involve photolysis reactions. In addition, its extremely short lifetime means that a clear diurnal cycle is observed for OH. It peaks during the noon at maximum sunlight and reduces to essentially zero at sun down. As mentioned in the beginning of this chapter, OH is an important atmospheric oxidant and alkene oxidation by OH primarily involves the preferential addition of OH to the less substituted carbon atom. This forms the more substituted, and consequently more stable, alkyl or allylic radicals. [26, 27]

Oxidation by the nitrate radical (NO_3) predominantly occurs during the night as the radical is rapidly photolyzed during the day due to its strong absorption throughout the visible region of the solar spectrum. [28]

$$NO_3 + h\nu \rightarrow NO + O_2 \tag{2.7}$$

$$NO_3 + h\nu \rightarrow NO_2 + O(^3P) \tag{2.8}$$

Sources of NO_3 radical in the troposphere are reactions between NO and NO_2 with O_3:

$$NO + O_3 \rightarrow NO_2 + O_2 \tag{2.9}$$

$$NO_2 + O_3 \rightarrow NO_3 + O_2 \tag{2.10}$$

Reactions 2.9 and 2.10 have rate coefficients of the order of 2×10^{-14} and 1×10^{-16} cm^3 $molecule^{-1}$ s^{-1}. [29]

NO_3 can react with NO_2 to form N_2O_5, which readily dissociates and establishes an equilibrium with NO_3. [28]

$$NO_3 + NO_2 + M \rightleftharpoons N_2O_5 + M \tag{2.11}$$

Nighttime NO_3 concentrations have been measured to be around 2.5×10^7 to 1.2×10^8 molecules cm^{-3} over the remote marine boundary layer and up to 1×10^9 molecules cm^{-3} in the semipolluted continental air masses. [28] The lifetime of the radical during the night is around 1400 h due to the low photolysis rate of 2×10^{-7} s^{-1} at full moon. [28] It should be noted that recent reports suggest that NO_3 can play a role also during the day. [30, 31]

Martínez et al. experimentally determined the rate constants of the reaction between NO_3 and a set of monoterpenes; 2-carene, sabinene, myrcene, α-phellandrene, d-limonene, terpinolene and γ-terpinene, at 298 K and found them to be between 9.4-52×10^{-12} cm^3 $molecule^{-1}$ s^{-1}. The lowest and highest rate constants corresponded to d-limonene and terpinolene, respectively. The reaction is predominantly via the NO_3 addition to the double bond. [32] Reaction via hydrogen abstraction is a relatively minor channel, but it leads to the formation of HNO_3 and peroxy radicals. [28, 33]

Tropospheric ozone (O_3) is mainly produced by the photolysis of NO_2.

$$NO_2 + h\nu \rightarrow NO + O(^3P) \tag{2.12}$$

$$O(^3P) + O_2 \rightarrow O_3 \tag{2.13}$$

Stratosphere-to-troposphere transport (STT) is an important source too, contributing to 13% and 34% of the lower and upper tropospheric ozone concentration, respectively. [34]

As can be seen in equations 2.1 and 2.2 and equations 2.9 and 2.10, O_3 is the main parent molecule of both OH and NO_3 radicals. As the major source of O_3, NO_2 is ultimately needed for oxidation. The main anthropogenic sources of NO_2 in the atmosphere are combustion of coal and oil. Lightning strikes can be an important natural source of NO_2. NO_2 is also generated by reactions of NO with peroxy radicals.

$$HO_2 + NO \rightarrow NO_2 + OH \tag{2.14}$$

$$RO_2 + NO \rightarrow NO_2 + RO \tag{2.15}$$

The lifetime of ozone in the troposphere ranges from a few weeks to a few months. [35] Typical ozone concentrations in the boreal forest conditions of Hyytiälä can reach levels of 40 ppb. [36] Reaction rate coefficients for VOC + O_3 reactions is dependent on the structure of the reacting VOCs. The cyclic monoterpenes α-pinene and β-pinene have reaction rate coefficients at 298 K of $\sim 8\times10^{-17}$ and $\sim 2\times10^{-17}$ cm^3 molecule^{-1} s^{-1}, respectively, for the reaction with O_3 [37] while the same for the linear β-ocimene molecule is $\sim 4\times10^{-16}$ cm^3 molecule^{-1} s^{-1}. [38]

The oxidation of alkenes by ozone addition is different to the addition reactions of OH and NO_3 described previously (see Figure 2.2). O_3 initially adds to the double bond, forming a constrained trioxide structure called the primary ozonide (POZ), which rapidly decomposes into a Criegee intermediate (CI; carbonyl oxide) and a stable carbonyl compound. The CI can be stabilized via collisions with other gas molecules. Stabilized CIs are important in the oxidative capacity of the atmosphere and SOA formation [39, 40, 41, 42] or it can isomerize via H-shift and form a (vinoxy-type) alkyl radical + OH. The alkyl radical can then add an O_2 in the atmosphere, forming a peroxy radical.

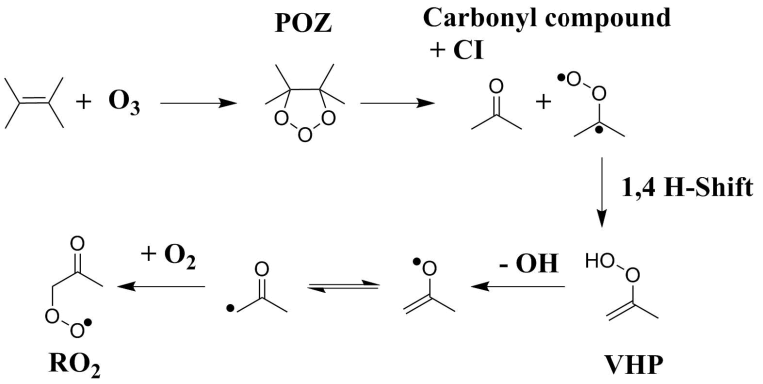

Figure 2.2: Ozonolysis reaction of an alkene. The primary ozonide (POZ) decomposes into a Criegee intermediate (CI) and a carbonyl compound. The CI forms a vinyl hydroperoxide (VHP) by a 1,4 hydrogen shift, followed by OH loss to form a vinoxy radical. The vinoxy radical then adds an oxygen molecule, forming a peroxy radical.

Due to their reactions with atmospheric oxidants, the lifetimes of BVOCs such as monoterpenes vary from minutes to few hours. [43] Some of the

radical products from the oxidation of VOCs that play an important role in gas-phase atmospheric chemistry are described in the following section.

2.2 Formation of peroxy and other important radical species in the atmosphere

Oxidation by OH, NO_3 and O_3 all result in the formation of an alkyl radical that rapidly adds an O_2 molecule in the atmosphere to form a peroxy radical (RO_2).

$$R^{\bullet} + O_2 + M \rightarrow RO_2^{\bullet} + M, \tag{2.16}$$

where M denotes air molecules that collisionally stabilize RO_2. The kinetics and mechanisms of the reactions of these peroxy radicals determine the primary oxidation products and their characteristic chemical behavior. Peroxy radicals can undergo multiple bimolecular sink reactions in the atmosphere with HO_2, NO and other RO_2, with generally applicable order-of-magnitude reaction rate coefficients of $\sim 1\times10^{-11}$, 1×10^{-11} and 1×10^{-12} cm^3 $molecule^{-1}$ s^{-1}, respectively, at 298 K. [44] Additionally, RO_2 + OH reaction has recently been suggested as an important sink for RO_2 and OH in pristine conditions [45, 46, 47, 48] with a fast reaction rate coefficient of $\sim 1\times10^{-10}$ cm^3 $molecule^{-1}$ s^{-1}. [44]

In pristine conditions with high VOC concentrations, RO_2 is mostly lost to reactions with HO_2 and other RO_2. Steady-state RO_2 concentrations in these conditions can be $\sim 1\times10^{9}$ molecules cm^{-3}. [49] In polluted environments, such as those in some of the mega-cities around the world, RO_2 is lost to reactions with NO. NO concentrations in the tens of parts per billion (ppb), which is common in some of the Chinese megacities, would translate to a steady state RO_2 concentration of $\sim 1\times10^{7}$ molecules cm^{-3}, two orders of magnitude lower than in pristine conditions. [50]

In addition to reacting with peroxy radicals, the HO_2 radical plays a very important role in combustion and atmospheric reactions. [51, 52, 53] It is generated in the atmosphere mainly by the reaction of the OH radical with CO:

$$OH + CO \rightarrow H + CO_2 \tag{2.17}$$

$$H + O_2 \rightarrow HO_2 \tag{2.18}$$

Another important source of HO_2 is from the reaction between alkoxy radicals (RO) and O_2. This channel is discussed in more detail in the

section discussing alkoxy radicals.

$$RO + O_2 \rightarrow R(O) + HO_2 \tag{2.19}$$

In low NO_x conditions, HO_2 is mainly lost to reactions with other peroxy radicals. Reactions with RO_2 can lead to radical and oxidant recycling in the atmosphere (see reactions 2.22 and 2.23).

$$HO_2 + HO_2 \rightarrow H_2O_2 + O_2 \tag{2.20}$$

$$HO_2 + RO_2 \rightarrow ROOH + O_2 \tag{2.21}$$

$$HO_2 + RO_2 \rightarrow RO^{\cdot} + OH + O_2 \tag{2.22}$$

$$HO_2 + RO_2 \rightarrow ROH + O_3 \tag{2.23}$$

The favorability of the three HO_2 + RO_2 reactions is dependent on the structure of the R-group in the RO_2 peroxy radical. For small RO_2 radicals, alkyl peroxy radicals predominantly undergo reaction 2.21. [54] Carbonyl containing acyl radicals can undergo all three reactions, while acetonyl radicals can undergo reactions 2.21 and 2.22. Reaction reaction 2.23 is only possible for acyl-type RO_2s. [55, 56, 57]

In polluted conditions, the HO_2 radical is primarily lost to reactions with NO, generating an OH radical and NO_2:

$$HO_2 + NO \rightarrow OH + NO_2 \tag{2.24}$$

Unimolecular H-shift reactions can often compete with the bimolecular RO_2 reactions in the atmosphere. [58, 59, 60] A unimolecular H-shift may be followed by additional H-shifts, adding an O_2 molecule in each step. This process is known as autoxidation [61, 20] and it leads to the formation of HOM that can potentially have very low volatilities and contribute to SOA formation. Figure 2.3 depicts the autoxidation process for a ketone compound. It should be noted that autoxidation is not the only unimolecular pathway a peroxy radical can follow and an H-shift reaction can quickly lead to the formation of a closed-shell product. Abstracting the H-atom from the carbon in the COOH group, for example, terminates the autoxidation process by forming a closed-shell carbonyl compound and releasing an OH.

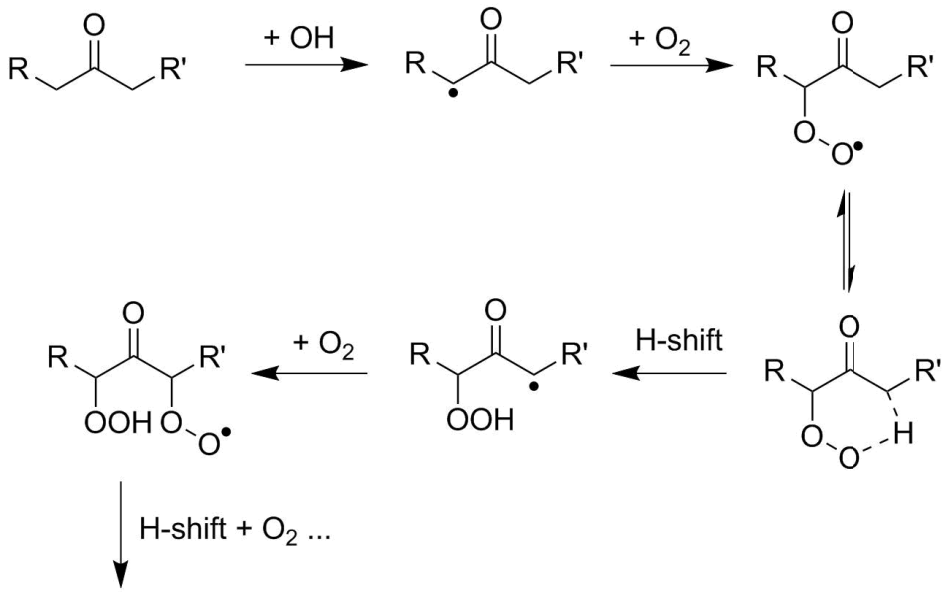

Figure 2.3: Schematic of autoxidation in OH-initiated oxidation of ketones. Following hydrogen abstraction by OH, the ketone adds an O_2 molecule to the radical carbon to form an RO_2. The RO_2 undergoes an H-shift isomerization to form a hydroperoxide and a carbon centered radical, which again adds an O_2 to form the next RO_2. This process can occur multiple times to form molecules with a high oxygen to carbon ratio.

Alkoxy radicals are key intermediates in the atmospheric degradation of VOCs and are the main subjects of **Article III** and **Article IV**. They are therefore discussed in detail here. In pristine conditions, alkoxy radicals are mostly generated from RO_2 + RO_2 and RO_2 + HO_2 reactions and in polluted environments by RO_2 + NO reactions. [62, 63] There are mainly three decomposition channels of alkoxy radicals in the atmosphere. First, unimolecular decomposition, which occurs through the breaking of the C-C bond adjacent to the oxy radical, producing a carbonyl compound and an alkyl fragment (see reaction 2.25). Second, alkoxy radicals can react with O_2, which leads to the abstraction of an α-hydrogen atom, generating a carbonyl compound and an HO_2 radical (see reaction 2.26). Third, alkoxy radicals are lost to unimolecular H-shift (isomerization) reactions (see reaction 2.27).

$$RO \rightarrow R^{'} = O + R^{''} \tag{2.25}$$

$$RO + O_2 \rightarrow R^{'} = O + HO_2 \tag{2.26}$$

$$RO \rightleftharpoons R^{'}OH \tag{2.27}$$

Due to their high loss rates (generally around $1{\times}10^4$ s^{-1} to $1{\times}10^6$ s^{-1} [63]), alkoxy radicals are assumed not to undergo bimolecular reactions in the atmosphere. However, a RO steady-state concentration of $1{\times}10^5$ cm^{-3} is possible in highly polluted environments (see **Article IV**) and, therefore, some bimolecular reactions involving alkoxy radicals can start to become non-negligible. The mechanism of a bimolecular reaction between organic peroxy and alkoxy radicals was explored in **Article IV**.

Monoterpenes constitute about 11% of the total annual BVOC emission, amounting to 83.6 Tg(C) $year^{-1}$. They include a number of compounds, all with the chemical formula $C_{10}H_{16}$, with different structural and chemical properties. On the basis of emission percentage, the five main monoterpenes are α-pinene, β-pinene, limonene, trans-β-ocimene and Δ^3-carene. In **Article III**, the primary RO_2 products from the oxidation of these monoterpenes with the oxidants OH, NO_3 and O_3 were studied. Depending on how the monoterpenes are oxidized and where the initial O_2 molecule adds, multiple RO_2 isomers are possible. **Article III** describes the effect of the different isomers and different conformers of a specific isomer on the reaction Gibbs energies of atmospherically relevant gas-phase radical reactions. It is important, therefore, that a distinction between an isomer and a conformer, concepts that are often erroneously interchanged, is clearly made.

Isomers are compounds with the same elemental composition but with different bonding patterns. One isomer cannot interchange with another, or, more precisely, interconversions between two isomers are generally associated with significant energy barriers as they involve the breaking and formation of covalent bonds. Conformers have the same elemental compositions and the same bonding patterns, and differ only in the three-dimensional arrangement of their atoms. Unlike isomers, the interconversion between conformers are generally not associated with large barriers as conformers only differ in the way the atoms are rotated around their bonds. While the definition of a conformer described here also fits stereoisomers, such as the R/S stereoisomery shown in Figure 2.4, the interconversion between R/S isomers are associated with the breaking of bonds (and are therefore isomers and not conformers). The different possible RO_2 isomers for OH-oxidized α-pinene system is shown in Figure 2.4. Four carbon-centered radicals are possible following the initial OH addition and a total of 8 peroxy radicals are possible following the addition of O_2.

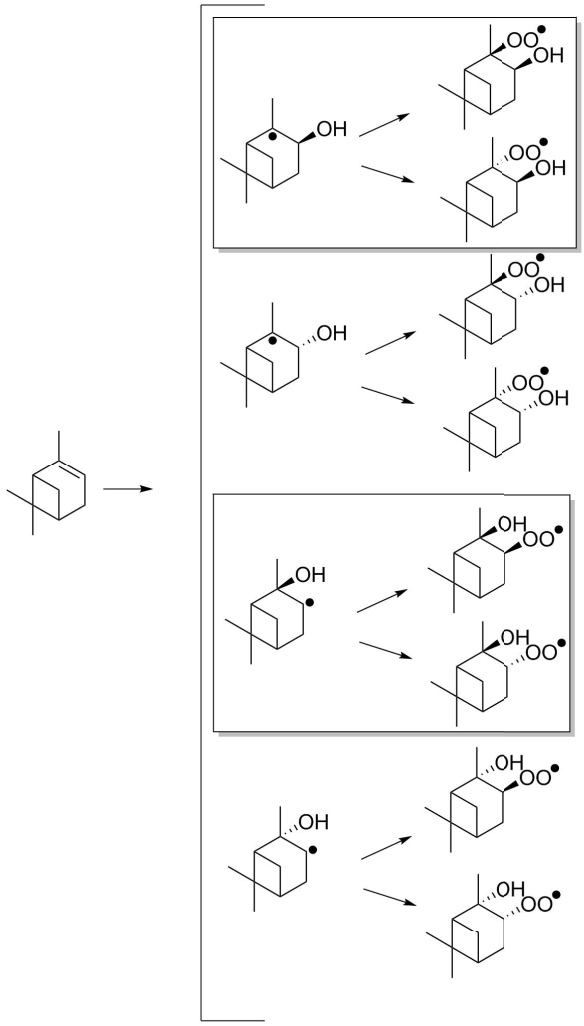

Figure 2.4: Possible peroxy radical isomers for OH-oxidized α-pinene system. There are four different possible alkyl radical isomers depending on the position of the OH attack and each alkyl radical in turn has two different RO_2 isomers, and therefore 8 possible RO_2 isomers in total.

Theoretical Background

3.1 Quantum Chemistry

The work that comprises this thesis relies on the properties of molecules that are calculated using quantum chemistry. These properties are derived from the wave function ψ. In calculations on molecular systems, this in practice usually means the employed basis set of atomic orbitals. The electronic ground state wave function should in principle include all the ground state information of the system under study in the non-relativistic limit and is obtained by solving the time-independent Schrödinger equation: [64]

$$\hat{H}\psi(R,r) = E\psi(R,r) \tag{3.1}$$

The Hamiltonian operator $\hat{H}$ describes the potential and kinetic energy of the system, the wave function $\psi(R,r)$ depends on the position of all nuclei (R) and electrons (r), and E is the total energy of the system with the wave function $\psi(R,r)$.

Equation 3.1 cannot be solved exactly for many-electron atoms or molecules, and some approximations need to be made to both the Hamiltonian (in practice, the treatment of electron correlation) and the wave function (in practice the employed basis set of atomic orbitals). The Hamiltonian accounts for the physical treatment of the system, electron correlation accounts for how the electrons interact with each other, and the basis set accounts for the flexibility of the solution (number of basis functions representing each atomic orbital).

Quantum chemical methods can be divided into wave function theory (WFT) and density functional theory (DFT). The former is definitely ab initio, which means that it does not require empirical data and can be solved from first principles. In the case of DFT, it is arguable whether it is ab initio as many DFT functionals are obtained by fitting to empirical data.

Certain approximations are adopted when calculating the molecular Hamiltonian using quantum chemical methods. The first is the Born-Oppenheimer (BO) approximation. [65] In this approximation, the position of the nucleus is considered fixed in order to solve the motion of the electron. This is reasonable as the light electrons move significantly faster than the heavier nuclei and can respond instantly to changes in the position of the nuclei. The Hamiltonian can consequently be separated into its electronic and nuclear components and the electronic part can be solved separately while keeping the nuclei position fixed.

$$\hat{H} = \hat{K}_N + \hat{H}_e + \hat{H}_{mp}, \tag{3.2}$$

where $\hat{K}_N$ is the nuclear kinetic energy operator, $\hat{H}_e$ is the electronic Hamiltonian, and $\hat{H}_{mp}$ is the mass polarization operator that arises because it is impossible to rigorously separate the center of mass motion from the internal motion in a system containing more than two particles. As the nuclei are assumed to be static, the nuclear kinetic energy operator can be neglected when solving the electronic wave function. The nuclear motion is accounted for in a subsequent step, typically by the rigid rotor harmonic oscillator approximation (RRHO). The mass polarization operator also disappears as it depends inversely on the total mass of the molecule and consequently its effect is negligible in most cases. With BO, the electronic wave function only depends on the electronic coordinates.

To better understand how this changes the molecular Hamiltonian, let us first look at the parameters that make up a molecular Hamiltonian:

$$\hat{H} = T_e + V_{e-e} + T_N + V_{N-N} + V_{e-N}, \tag{3.3}$$

where, T_e and T_N are the kinetic energy operators of the electrons and the nuclei, respectively. The rest describe the potential energy of the system; V_{e-N} describes the interaction of the nuclei with the electrons, V_{e-e} describes the interaction between the electrons, and V_{N-N} describes the interaction between the different nuclei. BO allows the electronic wave function to be solved for fixed nuclear positions. The nuclear coordinates are only parameters in the electronic Hamiltonian:

$$\hat{H}_e = T_e + V_{e-e} + V_{N-N} + V_{e-N}, \tag{3.4}$$

and in the corresponding wave function. The electronic Hamiltonian is solved for various nuclear coordinates to give a set of ground state electronic energies as a function of the nuclear coordinates.

Solving equation 3.1 exactly with the BO approximation is still impossible for many-electron systems and therefore, further approximations need to be introduced. This includes simplifying the electron correlation treatment and the use of finite basis sets.

Approximate solutions to the Hamiltonian with the BO approximation can be obtained by using the Hartree-Fock method (HF). In this method, the wave function is built from the products of single-electron wave functions. [66, 67] The wave function is represented as a single Slater determinant (SD) to satisfy Pauli's exclusion principle: [68]

$$\psi^{SD}(\vec{r_1}, \vec{r_2}, \cdots, \vec{r_N}) = \frac{1}{\sqrt{N!}} \begin{bmatrix} \varphi_1(\vec{r_1}) & \varphi_2(\vec{r_1}) & \cdots & \varphi_N(\vec{r_1}) \\ \varphi_1(\vec{r_2}) & \varphi_2(\vec{r_2}) & \cdots & \varphi_N(\vec{r_2}) \\ \vdots & \vdots & \ddots & \vdots \\ \varphi_1(\vec{r_N}) & \varphi_2(\vec{r_N}) & \cdots & \varphi_N(\vec{r_N}) \end{bmatrix}$$

The single-electron wave functions φ_i are called spin orbitals. In the non-relativistic approach, the spin is taken into account in a *ad hoc* manner. Each spin orbital consists of a spatial orbital that can include two spin states. For computation, the Schrödinger equation needs to first be manipulated. This can be done using variational calculus under the constraint that the spin orbitals remain orthonormal. The N-electron Schrödinger equation can be converted into N Hartree-Fock equations by minimizing the expectation value of the electronic energy, $\langle \psi^{SD} | \hat{H}_{elec} | \psi^{SD} \rangle$, with respect to the single-electron functions φ_i:

$$\begin{aligned} (\frac{1}{2}\nabla_i^2 - \sum_{\alpha=1}^{M} \frac{Q_\alpha}{\hat{r}_{i\alpha}})\varphi_i(\vec{r_1}) + \sum_{j=1}^{N} (\int \varphi_j^*(\vec{r_2}) \frac{1}{\hat{r}_{12}} \varphi_j(\vec{r_2}) \varphi_i(\vec{r_1}) d\vec{r_2} \\ - \int \varphi_j^*(\vec{r_2}) \frac{1}{\hat{r}_{12}} \varphi_i(\vec{r_2}) \varphi_j(\vec{r_1}) d\vec{r_2}) = \epsilon_i \varphi_i(\vec{r_1}), \quad (3.5) \end{aligned}$$

where, $i = 1 \cdots N$, ∇_i^2 operates on the electronic coordinates, M is the mass and Q is the atomic number of the nucleus α, $\hat{r}_{i\alpha}$ and $\hat{r}_{ij}$ are operators between electron i and nucleus α and the electrons i and j. The solution for any φ_i depends on the solutions of all the other φ_js. The equations must therefore be solved iteratively. This is done by converting the equations into a matrix form to be solved via matrix manipulation routines. [69] The

Hartree-Fock energy is obtained as:

$$E_{elec}^{HF} = \sum_{i}^{N} \epsilon_i - \frac{1}{2} \sum_{i=1}^{N} \sum_{j=1}^{N} (\int \varphi_i^*(\vec{r_1}) \varphi_j^*(\vec{r_2}) \frac{1}{\hat{r}_{12}} \varphi_i(\vec{r_1}) \varphi_j(\vec{r_2}) d\vec{r_1} d\vec{r_2} - \int \varphi_i^*(\vec{r_1}) \varphi_j^*(\vec{r_2}) \frac{1}{\hat{r}_{12}} \varphi_j(\vec{r_1}) \varphi_i(\vec{r_2}) d\vec{r_1} d\vec{r_2}), \quad (3.6)$$

where ϵ_i corresponds to the energy of an electron described by the single-electron wave function φ_i. Since HF is a variational method, the solution will provide the best possible one-determinant, non-interacting, independent particle approximation wave function ψ^{SD} in the average static Coulumb field, with the corresponding ground state energy E_{elec}^{HF}. While the HF method can recover up to 99% of the electronic energy of a system, it does not take into account electron correlation - the remaining 1%. Electron correlation can be dynamic, which is the rapid response of electrons to the movement of other electrons around them, and static, which comes from the near degeneracy of electronic configurations. The lack of electron correlation treatment has a significant impact on chemistry as without the ability to respond to the movements of other nearby electrons, the electrons are predicted to be too close to each other, resulting in bond lengths that are too short. Also, bond energies are often very wrong. For chemistry, getting accurate bond energies is paramount.

To account for electron correlation, the wave function can be constructed using more Slater determinants, each with a specific electron configuration. The different electron configurations are obtained by moving electrons from occupied orbitals to unoccupied orbitals, called excitations. The excitations can be single, double, triple, etc. depending on how many electrons are excited in all possible combinations. The new wave function is then optimized as a function of the total energy.

Methods that account for electron correlation are called post-HF methods and include: Configuration Interaction (CI), Coupled Cluster (CC) and Many-Body Perturbation Theory (MBPT) methods. Out of these, CC based methods are the most successful. [70, 71] The CC method describes the wave function as:

$$\Psi_{CC} = e^{\hat{T}} \phi_0 \quad (3.7)$$

where $\hat{T}$ is the cluster operator and is a sum of all possible excitation operators ($\hat{T} = \hat{T}_1 + \hat{T}_2 + \cdots$; $\hat{T}_1$ contains single excitations, $\hat{T}_2$ contains double excitations, and so on). The $e^{\hat{T}}$ function can be expanded as a Taylor

series:

$$e^{\hat{T}} = 1 + \hat{T} + \frac{\hat{T}^2}{2!} + \frac{\hat{T}^3}{3!} + \cdots \tag{3.8}$$

The cluster operator $\hat{T}$ can be expanded to include all the possible excitations:

$$e^{\hat{T}} = 1 + \hat{T}_1 + (\frac{\hat{T}_1^2}{2!} + \hat{T}_2) + (\frac{\hat{T}_1^3}{3!} + \hat{T}_1\hat{T}_2 + \hat{T}_3) + \cdots \tag{3.9}$$

The excitation operator $\hat{T}_n$ contains all the nth order excitations. The CC method provides the exact solution of the time-independent Schödinger equation when all the excitations are included. The series expansion can be truncated to include only specific electron excitation operators. The inclusion of only the double excitations, or CCD, is the simplest way to improve the HF result.

The CC method is generally not considered to be variational as the CC wave function can only be solved variationally for small systems. [72] The canonical CCSD(T) with the single, double and perturbative triple excitations is the commonly used highly accurate post-HF method. This method is only suitable for small systems as the calculation time scales N^7, where N is the system size defined by the number of basis functions. Basis functions are described in detail later in the chapter. The steep scaling issue can be avoided by making local approximations and by introducing terms into the wave function that depend explicitly on interelectronic coordinates. F12 CC methods have been shown to have improved basis set convergence compared to the canonical CC methods by including interelectronic distances in the methods. [73] This means that smaller basis sets can be used to achieve a similar level of accuracy as the canonical CC methods. The recently introduced domain-based local pair natural orbital (DLPNO), [74] a development in the local correlation methods, shows a near linear scaling of computational time with system size, making it suitable for large systems. Instead of canonical delocalized orbitals, the DLPNO method uses pair natural orbitals (PNO) that are localized and classified into domains. The most important excitations that account for electron correlation are then selected. The DLPNO-CCSD(T) method is reported to recover 99.6% of the correlation energy of the canonical CCSD(T). [74] It should be noted that while the coupled-cluster component of a DLPNO calculation scales linearly, the initial HF calculation needed scales to N^4.

3.2 Density functional theory

Density functional theory (DFT) relies on the fact that the ground state electronic energy can be determined completely by the electron density. The notion that the energy of a molecule can be expressed in terms of its electronic density dates back to the early works of Dirac, [75] Fermi, [76] Thomas, [77] and Wigner. [78] Hohenberg and Kohn provided the formal proof of this notion in 1964, [79] although the exact functionals that connect the kinetic and electron-interaction energies to the electron density are still unknown.

Kohn and Sham provided the set of self-consistent equations that are to be solved to find a set of spin orbitals that are the basis of modern KS-DFT methods: [80]

$$E_{DFT}[\rho(r)] = T_e[\rho(r)] + J_{ee}[\rho(r)] + V_{Ne}[\rho(r)] + E_{xc}[\rho(r)]. \tag{3.10}$$

This equation connects the electron density to the energy of the system. $T_e[\rho(r)]$ describes the kinetic energy of the system, J_{ee} the Coulomb electron-electron repulsion, V_{Ne} is the nuclear-electron attraction term, and E_{xc} is the exchange correlation functional. The kinetic energy T_e is described by considering the electrons as non-interacting, but having the same electron density as the true system of interacting electrons. E_{xc} corrects the approximations made to the kinetic energy and the electron correlation to give the exact solution. A disadvantage of the KS-DFT method is that the exact value of E_{xc} is not known. Practical K-S DFT calculations use different approximations for it.

Solving the KS equations involves the solving of the orbitals that minimize the energy of the system. While in the HF method the electrons interact with the effective field that describes the average positions of the electrons, in DFT, the electrons interact with the potential constructed from the electron density of non-interacting electrons, with the same density as the real system of interacting electrons.

3.3 DFT functionals

Accuracy of DFT methods depends on the exchange-correlation functional. Since the exact functional is not known, several approximate functionals

have been developed. Commonly used approximate DF functionals are local density approximation (LDA), generalized gradient approximation (GDA), meta-GDA and hybrid and double-hybrid functionals. There are currently a huge number of GGA and hybrid functionals available and this makes choosing an appropriate functional for the job at hand and comparisons between functionals difficult.

3.3.1 LDA functionals

The LDA approximates the exchange-correlation energy density at a specific position to be a function of the electron density at that position. It is assumed that the density is a slowly varying function. As typically electron density is far from being spatially uniform in real chemical systems, the usefulness of LDA is rather limited. However, it is useful for modeling periodic metal systems where the electron density varies gradually.

3.3.2 GGA and meta-GGA functionals

The LDA description can be improved by including the first derivative, or the gradient, of the electron density in the electron-correlation functional. The resulting generalized gradient approximation (GGA) represents a significant improvement over the LDA. Examples of GGA functionals are BP86 [81, 82] and PBE [83]. The functional can be further improved by including higher order derivatives of the electron density or on the local kinetic energy density. Meta-GGAs have been shown to be a slight improvement over GGAs with similar computational costs. [84]

3.3.3 Hybrid and double-hybrid functionals

Hybrid functionals are formed by combining the GGA and meta-GGA functionals with some of the exact electron exchange energy from the HF theory. B3LYP is a popular hybrid functional which combines the Becke-3-parameter exchange functional with Lee-Yang-Parr correlation functional. [85, 86]

Double-hybrid functionals include a fraction of MP2-correlation energy into the hybrid functional in order to account for the virtual orbitals. An example of such a functional is B2PLYP. [87]

3.3.4 Dispersion Corrections

Long-range dispersion interactions arise from electron correlation in wave function methods, but are poorly described by most DFT funtionals. [88] The quality of modeling dispersion effects is highly functional dependent. While functionals such as PW91 provide at least qualitatively correct interaction potentials for some van der Waals complexes, other functionals such as B3LYP predict purely repulsive potentials. [89] Minnesota functionals, such as M06-2X, have been parametrized to model dispersion interactions. [90]

The dispersion interactions are included as an external correction in most of the current dispersion-corrected methods. The DFT-D approach suggested by Grimme treats dispersion as an additional emperical term to the DFT energy: [91]

$$E_{DFT-D} = E_{DFT} + E_{disp} \tag{3.11}$$

where, E_{DFT} is the DFT energy and E_{disp} is the dispersion term. The add-on dispersion term does not directly alter the wave function, electron density or any other molecular properties. However, the geometries following optimizations with and without dispersion corrections are different as the former contributes to forces acting on atoms. [92] Range-separated hybrid-GGA functional ωB97X-D developed by Mardirossian and Head-Gordon contains ten parameters and non-local correlation effects. [93] It has been shown to produce good structures and thermochemical parameters for non-covalently bound molecular clusters. [94, 95, 96]

3.4 Basis sets

In the quantum chemical methods employed in this work, the electronic structure of the studied molecules are optimized by first placing the electrons in molecular orbitals that are constructed from a linear combination of atomic orbitals. Each one-electron wave function (ϕ) can be written as a linear combination of basis functions (χ):

$$\phi = \sum_i a_i \chi_i, \tag{3.12}$$

where a are the coefficients that are solved in the calculation. In calculations on molecular systems, the two most common basis function types are Slater-type orbitals (STOs) and Gaussian-type orbitals (GTOs). Other types include plane waves, grids and wavelets. The STO mimics the exact solution

of the Schrödinger equation for the hydrogen atom:

$$\chi_{\zeta,n,l,m(r,\theta,\phi} = NY_{l,m}(\theta,\phi)r^{n-1}e^{-\zeta r}, \tag{3.13}$$

where, N is the normalization constant, $Y_{l,m}$ are the spherical harmonic functions that depend on the angular moment quantum numbers l and m, n is the principle quantum number, ζ controls the width of the orbital, and r, θ and ϕ are the polar coordinates. STO has a direct physical interpretation for molecular orbitals. However, most of the required integrals in the SCF procedure are calculated numerically, which drastically increases the computational work load.

GTO are approximations of the orbitals of a hydrogen atom:

$$\chi_{\zeta,n,l,m}(r,\theta,\phi) = NY_{l,m}(\theta,\phi)r^{2n-2-l}e^{-\zeta r^2}, \tag{3.14}$$

STOs can be approximated as linear combinations of GTOs. Unlike STOs, because the product of two GTOs can be written as a linear combination of the GTOs, integrals with the Gaussian basis functions can be written in closed form. This drastically reduces the computational time. However, a single GTO does not correctly describe the solution of a one electron atom and multiple GTOs are needed to describe one basis function. Each STO, on the other hand, correspond to a basis function. The computational methods used in this work all use GTOs to construct the basis functions.

3.4.1 Basis set sizes

The smallest possible basis set, called the minimal basis set, has one basis function for each atomic orbital. For example, consider the electron configuration of carbon, i.e. $1s^2 2s^2 2p^2$. To satisfy the minimal requirement, the basis set for carbon should include two s-type functions ($1s^2$ and $2s^2$) and three p-type functions (p_x, p_y and p_z). Each basis function contain multiple GTOs. A basis set that fulfills this minimal condition is called a single-ζ (SZ) basis set. As can be inferred, a basis set that satisfies the minimal requirement is not very accurate, especially when dealing with delocalized valence electrons. Adding more basis functions per atomic orbital is a straightforward method to increase the accuracy of the computation. A double-ζ (DZ) basis set has two basis functions describing each occupied atomic orbital. For the carbon atom, the DZ basis set will have a total of 10 basis functions (4 s-type and 6 p-type). Similarly, the accuracy can be improved further by using basis sets that are triple-ζ (TZ), quadruple-ζ (QZ) and so on. The computational effort and time increases rapidly with

the increase in the number of basis functions used. In order to increase the accuracy of the calculation while not allowing the computational cost to get out of hand, split-valence basis sets were introduced. These basis sets treat the core and valence electrons separately. The minimal basis set requirement is satisfied for the core electrons, while more basis functions are used to treat the more chemically important outer valence electrons. Additionally, polarization and diffusion functions are added to allow more flexibility for the electrons to delocalize. For the former, functions with an angular moment one greater than the valence space is added. Not doing so for the hydrogen atom, for example, will lead to the electron distribution to be always spherical, and will neglect the fact that in real molecules, the hydrogen atoms are polarized. By adding addition p-type functions, the polarization effect for hydrogen atoms is taken into account. Diffuse functions are used to allow the outer electron space to expand (important for anions, for example).

3.5 Cluster thermodynamics and kinetics

The free energies, enthalpies and other thermochemical properties reported in the studies that comprise this thesis are obtained after the ground state electronic energies at $T = 0K$ are calculated using the electronic structure calculations discussed above. The different energetic contributions from the translational, vibrational, and rotational degrees of freedom of molecular systems are first assumed to be uncoupled. The total energy (ϵ_{tot}) can be written as the sum:

$$\epsilon_{tot} = \epsilon_{el} + \epsilon_{tr} + \epsilon_{vib} + \epsilon_{rot}, \tag{3.15}$$

where ϵ_{el} is the electronic energy, ϵ_{tr} is the translational energy, ϵ_{vib} is the vibrational energy and ϵ_{rot} is the rotational energy. The total partition function of the system is expressed as:

$$q_{tot} = q_{el} \times q_{tr} \times q_{vib} \times q_{rot}. \tag{3.16}$$

The total Gibbs free energy G_{tot} of the system is related to the total enthalpy H_{tot} and total entropy S_{tot} as:

$$G_{tot} = H_{tot} - TS_{tot} \tag{3.17}$$

The total enthalpy and entropy is expressed as the sum of the corresponding electronic, translational, vibrational, and rotational contributions. Each

component of the enthalpy (H_X) is calculated from the corresponding partition function component:

$$H_X = k_B T^2 (\frac{\partial \ln q_X}{\partial T})_V + k_B T V (\frac{\partial \ln q_X}{\partial V})_T. \tag{3.18}$$

Similarly, for entropy (S_X):

$$S_X = k_B T (\frac{\partial \ln q_X}{\partial T})_V + k_B \ln(q_X). \tag{3.19}$$

Here q_X is the partition function of either electronic, translational, vibrational, or rotational degree of freedom, k_B is the Boltzmann constant, T is the temperature and V is the volume.

The rigid rotor harmonic oscillator (RRHO) approximation is generally used to calculate vibrational frequencies. The approximation assumes molecules behave as equilibrated ideas gas particles and temperature is taken into account by assuming that the molecular structures vibrate harmonically about their equilibrium geometries and all rotational modes are rigid. The RRHO approximation is not always appropriate for all vibrational modes of large molecules and for hydrogen bonded clusters.

Computational methods described thus far in this chapter were used to compute both the thermodynamics and the kinetics of reactions. It is important, therefore, to make a concrete distinction between the two concepts. A good rule of thumb in physical chemistry is that the feasibility of a reaction cannot be determined only from thermodynamics; reactions that are thermodynamically favorable can still have kinetic barriers that restrict them. The clusters calculated in **Articles I** and **II** were formed without kinetic barriers, and their stabilities can therefore be ascertained from just thermodynamics. The formation of a cluster C, for example, by the association of reactants A and B at thermodynamic equilibrium is given by:

$$\mathrm{A} + \mathrm{B} \rightleftharpoons \mathrm{C} \tag{3.20}$$

The formation free energy of C, ΔG is given by:

$$\Delta G = \Delta H - T\Delta S, \tag{3.21}$$

where, ΔH is the change in enthalpy, ΔS is the change in entropy and ΔG = $G(C)$ - $G(A)$ - $G(B)$.

Both the enthalpy and the entropy decreases during the clustering process; the enthalpy decreases as the formation of the H-bonded clustering process is exothermic, and the entropy decreases as going from free reactants to a H-bonded cluster essentially reduces the number of degrees of freedom. This implies that for a cluster forming reaction to be feasible, i.e. $\Delta G < 0$, the intramolecular interactions in the cluster need to overcome the entropy penalty.

Reactions with kinetic barriers were studied in **Articles III** and **IV**. Kinetic barriers, or transition states (TS), are first-order saddle points on the potential energy surface. A saddle point is a local maximum along one coordinate and minimum in all other coordinates. The breaking of covalent bonds are usually associated with a TS. As in the clustering process explained above, the TS complex also experiences an entropy penalty relative to the separated reactants (and products) and a decrease in enthalpy from favorable intra-molecular interactions. By calculating the two parameters, the Gibbs free energy of the TS can be found using equation 3.21. This was exactly what was done in **Article III**. Because the studied systems were quite large (monoterpene derived molecules), only the reaction free energies were calculated for the reaction $RO_2 + HO_2 \rightarrow RO + OH + O_2$. The entropy penalty and the enthalpic contributions to the TS for a smaller but similarly functionalized "R" relative to the products was calculated. This was then used to approximate the rate-limiting TS of the actual monoterpene-derived systems.

The approach of estimating the TS energy from the overall reaction energy is not novel and is similar to the Brønsted-Evans-Polanyi (BEP) principle. [97, 98, 99] The BEP principle postulates that, for an elementary reaction, there exists a linear relationship between the activation barrier and the reaction energy. It should be noted that the reactions in **Article III** are not elementary as they involve multiple intermediate and transition state complexes along the reaction coordinate. The entire reaction pathway for alkyl, acyl and acetonyl $RO_2 + HO_2$ reaction are provided by Hasson et al. [57]

Mass Spectrometry

Mass spectrometry requires that the gas-phase sample is ionized (positively or negatively charged) and isolated electrically or magnetically by its mass-to-charge ratio. The idea of mass spectrometry is relatively old; it was originally put forth by J. J. Thomson as far back as 1913. [100] The first prototype of modern static magnetic mass spectrometers was built by E. W. Aston in 1919. [101]

In the past three decades, the field of mass spectrometry has evolved and has found applications in a multitude of disciplines that covers physical, life and health sciences. [102, 103, 104] Mass spectrometers are used by astronomers to detect the constituents of solar wind [105] and the atmospheres of other celestial bodies in the solar system, [106] by environmental scientists to detect toxins in contaminated fish, [107] by biologists to identify the composition of structures of complex molecules such as carbohydrates, proteins, and nucleic acids, [108, 109] and many more.

In this thesis, we focus on the use of mass spectrometers in studying important trace gas molecules in the atmosphere; in particular, a chemical ionization atmospheric pressure interface time of flight mass spectrometer (CIMS).

4.1 Components of a mass spectrometer

A mass spectrometer can be divided into three main components: ionizer, mass analyzer, and detector. Ionization methods employed by mass spectrometers can be broadly divided into "hard" and "soft" techniques. "Hard" ionization techniques, such as electron ionization, impart high energy (commonly ∼70 eV or ∼6754 kJ/mol in electron ionization) [110] to the sample molecules during the ionization process and can lead to the

fragmentation of the sample. "Soft" ionization methods, on the other hand, impart relatively little energy during ionization and are therefore unlikely to lead to fragmentation. Examples of soft ionization techniques include electron spray ionization (ESI), matrix-assisted laser desorption ionization (MALDI), chemical ionization (CI), and others. Minimal sample fragmentation during the ionization process is important when studying complex molecules as this simplifies species identification, and the "soft" ionization technique is therefore often preferred when studying atmospheric trace gases.

The mass analyzer component of the instrument separates the ions based on their mass to charge (m/z) values. The popular mass analyzers that are currently used are quadrupole (Q), quadrupole ion trap (QIT), time-of-flight (TOF) and Fourier transform ion cyclotrone resonance (FT-ICR). The different analyzers vary in their resolution and mass range. The quadrupole analyzer consists of four parallel electric rods; a direct current potential (U) is applied to two of the rods and other two are linked to an alternating radio-frequency (with frequency ω potential (V). From the ionizer, the ions are directed towards a quadrupole by an electric field. A negatively charged ion, for example, will move towards the positively charged quadrupole. Changing the polarity will induce the ion to change its path before striking the quadrupole. The ions will therefore undergo a complex oscillatory trajectory and by controlling the values U, V and ω, ions within a narrow m/z range can be transmitted towards the detector. The advantages of the quadruple analyzer include low cost, small size and an ease of maintenance. However, they have a limited mass range of less than 4000 Th and low resolving power. The unit Thomson (Th) is the unit of mass/charge. 1 Th $= 1\text{u/e} = 1.0364 \times 10^{-8}$ kg/C.

The instrument discussed in the articles comprising this thesis has a TOF analyzer and is described in the following section.

4.2 Chemical ionization atmospheric pressure interface time of flight mass spectrometer (CIMS)

A chemical ionization atmospheric pressure interface time of flight mass spectrometer (CIMS) was used in the experimental work described in this thesis. The atmospheric pressure interface enables the sampling of the ambient gases without pretreatment, allowing for direct online measurement. Since the ionization occurs at atmospheric pressure, the efficient sampling of ions into vacuum can be an issue. The CIMS instrument consists of

four differentially pumped chambers; the first two chambers contain short segmented quadrupoles used for guiding the ions, the third contains an ion lens assembly, and the fourth is a TOF analyzer. The first chamber is maintained at a pressure of around 2 mbar by using a scroll pump. The scroll pump is also used as the backing pump for a turbo pump. The turbo pump reduces the pressure inside the mass spectrometer further, with a typical final pressure inside the TOF region of 1×10^{-6} mbar [111] (1 mbar = 100 Pa).

The TOF relies on mass separation at the detector following the free flight of ions of different masses. Two ions on a path towards the detector that are formed at the same time, have the same charge, but differ in their masses reach the detector at different times. The mass to charge m/z ratio is a function of the time-of-flight: [112]

$$m/z = 2Est_f^2/(2s + x)^2, \tag{4.1}$$

where E is the applied voltage, s is the length of the ion acceleration region, t_f is the total time of flight and x is the length of the flight path. Theoretically, E, s and x are fixed. Equation 4.1 can be reduced to:

$$m/z = Kt_f^2, \tag{4.2}$$

where, K is the calibrating factor. The TOF instrument can detect a high mass range, and has a high resolution due to the use of electrostatic ion mirrors that reflect the ions and increase the flight path length to the detector. The ion flight path can be run in either of two modes, V or W. The letters illustrate the flight paths of the ions inside the TOF. The shorter flight path V was used in the experimental work reported in this thesis. It has a resolving power of 3000 Th/Th, which is defined as

$$R = M/\Delta M,$$

where M is the mass/charge ratio and ΔM is the peak width at the half maximum.

An illustration of a typical CIMS instrument is shown in Figure 4.1.

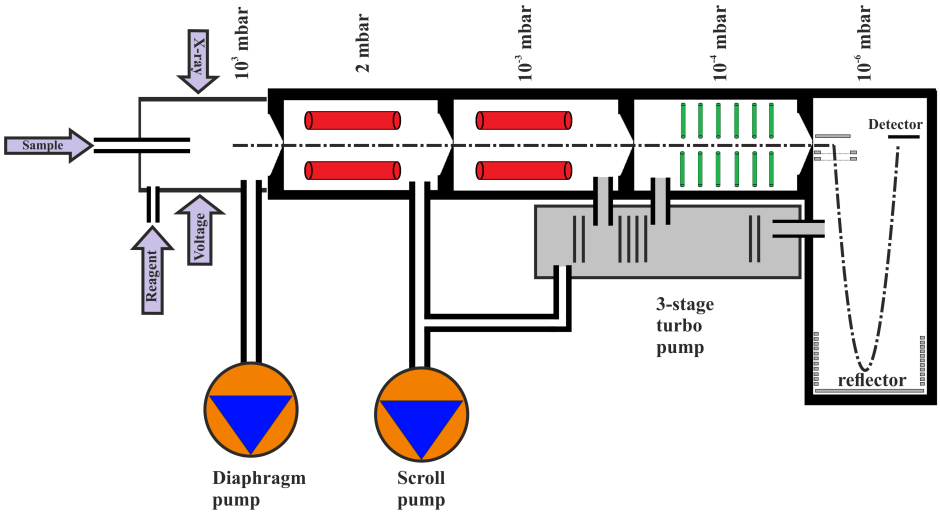

Figure 4.1: A typical TOF CIMS instrument. The first section of the TOF-MS is pumped with a scroll pump, while the other chambers are pumped using a 3-stage turbo pump. The ion guides include the (red) quadrupoles and the (green) ion lens stack and they guide the ions to the TOF region.

4.2.1 Ionization

Mass spectrometers that utilize the chemical ionization method to detect sample molecules have become increasingly useful in the detection of atmospheric trace gases. These instruments offer high sensitivity and a range of selectivity that depends on the type of reagent ion used for chemical ionization. These properties are especially important as the molecules that play a crucial role in atmospheric reactions vary in structure and functionalities and generally have very low concentrations. In chemical ionization using a reagent ion, the sample molecules are allowed to interact with the reagent ion stream for a short time (∼200 ms) in the ion-molecule reaction (IMR) region before being guided towards the mass analyzer. The analyte molecules are ionized in multiple ways, such as charge transfer, protonation, deprotonation, cluster formation, among others. In **Articles I, II** and **V**, the analytes were ionized primarily through cluster formation with the analyte·reagent ion cluster held together by hydrogen bonds.

The reagent ions that were studied in this work were all negatively charged ions (anions). Iodide (I^-) and nitrate (NO_3^-) anions have one or multiple hydrogen bond acceptor groups and are able to ionize those analytes that have have at least one or multiple hydrogen bond donating groups. I^- can ionize certain molecules in ways other than forming H-bonded clusters and these will be described in the following section. Hydrogen bond donating groups are usually hydroxy, hydroperoxy, carboxylic acid, or peroxy acid groups, while the hydrogen bond acceptor groups in the reagent ion are usually oxygen or halogen atoms. The sensitivity of the CIMS methods that rely on ionization via hydrogen bonded cluster formation is dependent on the binding strength of the cluster. Weakly bound clusters are more likely to dissociate inside the IMR region than the more strongly bound clusters. This directly affects instrument sensitivities.

Picking the right reagent ion

In studies that are focused on detecting and quantifying atmospherically relevant gas-phase molecules, CIMS has proven to be indispensable. However, choosing the right reagent ion is important as it directly translates to what molecules can be efficiently detected. The nitrate ion is highly selective and is the preferred reagent ion for detecting gas-phase sulfuric acid (H_2SO_4) [113, 114, 115, 116], which is detected as the bisulfate ion (HSO_4^-) via the following reaction in the ion-molecule reaction chamber of the CIMS:

$$H_2SO_4 + NO_3^- \rightarrow HSO_4^- + HNO_3 \tag{4.3}$$

While the sensitive detection of gas-phase sulfuric acid was pivotal in popularizing the nitrate reagent ion, it was its high sensitivity and selectivity towards the higher oxidized SOA precursor molecules that established it as the standard CIMS method in the atmospheric science community. [18, 19, 117, 118] The nitrate ion was found to be strongly selective towards the highly oxidized molecules (with oxygen:carbon atom ratios close to 1 or higher). This is due to the strong binding free energy of 84.2 kJ/mol [119] of $HNO_3 \cdot NO_3^-$, causing the majority of the nitrate reagent ions to exist in the dimer form in the ion molecule reaction chamber of the instrument. Only those analyte molecules that can bind to NO_3^- stronger than HNO_3 are able to steal the charge (and subsequently be detected by the instrument) via ligand-exchange reactions. This is illustrated in equations 4.4 and 4.5. The higher oxidized molecules often contain at least two hydrogen bond donating groups, a characteristic known to lead to a stronger binding with the NO_3^- anion. [120]

$$NO_3^- + HNO_3 \rightleftharpoons HNO_3 \cdot NO_3^- \tag{4.4}$$

$$HNO_3NO_3^- + analyte \rightleftharpoons HNO_3NO_3^- \cdot analyte \rightleftharpoons HNO_3 + analyte \cdot NO_3^- \quad (4.5)$$

The high selectivity of the nitrate ion towards molecules with multiple H-bonding groups makes it a poor choice for studying molecules such as carboxylic acids, halogen oxides, and precursor molecules involved in the formation of the higher oxidized molecules. [121, 122, 123, 124]

In contrast, acetate-CIMS is a lot less selective as the reagent dimer is less strongly bound than the nitrate dimer (∼74 kJ/mol in this case). This means that some of the less oxidized species can have a sufficiently strong binding free energy to $CH_3C(O)^-$, enabling them to steal the ion from acetic acid by ligand-exchange reactions. [125] A less selective reagent ion like the acetate anion is beneficial as it extends the list of molecules that can efficiently be detected. [125, 126, 127, 128, 129]

Because nitrate- and acetate-CIMS have stable reagent ion dimers, and the sensitivity of the two methods depends on efficient ligand-exchange reactions between the reagent ions and the target molecules, they have negligible humidity dependence. [120] In their computational study that compared the charging of butadiene (isoprene surrogate) oxidation products by different reagent ions, Hyttinen et al. found that water binds weakly to nitrate and acetate reagent ions (relative to the respective reagent ion dimers). [120]

Another popular negative reagent ion in CIMS is the iodide anion. It has been used to efficiently detect small carboxylic acids and halogen compounds. [130, 131, 132, 133] The iodide anion has a large negative mass defect (difference between the nominal integer mass and the exact mass of a molecule) of -0.096. This helps differentiate between the iodide-clustered and the non-iodide-clustered peaks in the iodide-CIMS mass spectra, making the analysis of the spectra easier. Like the acetate ion, iodide can cluster with the less oxidized molecules. Unlike acetate and nitrate, however, iodide does not form high steady-state concentrations of $I{\cdot}I^-$ dimers. This makes this method more susceptible to humidity effects (despite the binding free energies of I^- with one to three water molecules being systematically lower than those for NO_3^- and $CH_3C(O)O^-$, see Hyttinen et al. [120]). Iodide-CIMS primarily charges sample molecules by forming H-bonded molecule$\cdot I^-$ clusters and can therefore only detect molecules that contain at least one H-bond donating group. Certain subset of molecules, under the right conditions, can react with the iodide anion in the CIMS inlet and produce non-clustered organic ions. Peroxy acids (reaction 4.6) and

peroxy radicals (reaction 4.7) can decompose into carboxylate ions in water catalyzed reactions with I^-.

$$RC(O)OOH + I \cdot H_2O^- \rightarrow RC(O)O^- + HOI + H_2O \quad (4.6)$$

$$RC(O)OO + I \cdot H_2O^- \rightarrow RC(O)O^- + IO + H_2O \quad (4.7)$$

The bromide-CIMS method with the Br^- reagent anion has recently garnered interest and is reportedly very adept at detecting the hydroperoxyl radical (HO_2) [134, 135]. Like iodide-CIMS, the reagent ions primarily exist as monomer Br^- inside the IMR, and therefore the method has a humidity dependence. The humidity dependence of Br-CIMS is reportedly stronger than that of iodide-CIMS because of the stronger binding energy of Br^- with water. [120] In **Article V**, we demonstrate the ability of the Br-CIMS method in detecting the oxidation products of α-pinene and cyclohexene.

The inability of one particular CIMS method to identify a wide mass range of atmospherically relevant gas-phase molecules typifies the limitations of using single reagent ions. One way to circumvent the blind-spots inherent in a single reagent ion CIMS method is to use multiple reagent ions in parallel. A comparison between the nitrate- and iodide-CIMS was drawn in **Article II** by considering the detection of the well-established cyclohexene ozonolysis products. In that experimental work, we lacked the means to run the two ion-modes concurrently, and the experiments were therefore performed twice, once for each reagent ion, in identical conditions. In **Article V**, a new multi-scheme chemical ionization inlet (MION) was used that could switch between two reagent ions (nitrate and bromide in this case) within a second time-scale, allowing us to detect α-pinene and cyclohexene ozonolysis products by both reagent ions in a single experiment. While **Article V** only reports the switching between two reagent ions, multiple reagent ions can be fed into the MION inlet, thereby greatly increasing the number of molecules that can potentially be detected.

4.3 Sensitivity of a CIMS instrument

For CIMS methods that ionize sample molecules via molecule·reagent ion cluster formation, their sensitivity for a molecule X depends on the successful transmission of the X·reagent ion cluster to the detector.

The transmission of ion clusters in a CIMS instrument involves passing through the ion optics of the instrument. This imparts energy on the clusters via electric fields. A strongly bound cluster should fare better

than those that are less strongly bound and should therefore be detected at a relatively high sensitivity. Weakly bound clusters will inevitably have faster fragmentation rates and are consequently detected at low sensitivities. Figure 4.2 illustrates the dominant fates of strong and weakly bound clusters inside a CIMS.

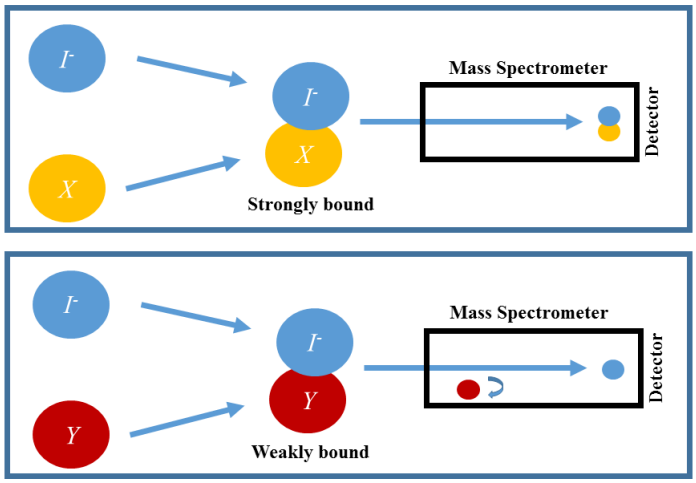

Figure 4.2: Illustration of strong and weak clustering of sample molecules X and Y with the reagent ion I^-. The stronger $X \cdot I^-$ cluster survives the journey through the mass spectrometer to the detector, while the weaker $Y \cdot I^-$ cluster fragments and is therefore undetected. A weaker cluster binding energy leads to the fragmentation of more clusters, and this has a direct relation to instrument sensitivities.

4.3.1 Translating binding energies into approximate instrument sensitivities

The detection efficiency of a CIMS instrument for a particular analyte depends on whether the analyte·reagent ion cluster remains whole long enough to reach the detector. More the number of analyte·ion clusters that reach the detector intact, higher the sensitivity of the instrument for that particular analyte. The fate of these clusters can be numerous - analyte and the ion could undergo a chemical reaction forming entirely different species to the analyte that was initially sampled, the cluster could lose its charge,

and therefore be undetected, or the cluster could fragment back into the original constituents. The sensitivity of the CIMS should increase with the collision rate between the analyte and the reagent ion and decrease with fragmentation or any other mechanism that limits the detectibility of the molecule. The collision rates between a particular reagent ion and a neutral molecule likely does not depend greatly on their identities. This was checked for the I^- reagent ion and a set of atmospherically relevant carboxylic and dicarboxylic acids in **Article I**. The collision rates were found to be within an order of magnitude of each other. Therefore, CIMS sensitivity is likely mainly controlled by cluster fragmentation. If we consider that the particular chemical ionization method is entirely "soft" (i.e. the reagent ion binds with the analyte without fragmenting or reacting with it), the fragmentation of the cluster back into the analyte and the reagent ion inside the IMR should be related to the binding energy of the cluster.

The mechanism of fragmentation depends on at least three different cases:

1. Near-immediate fragmentation of the formed cluster in the IMR region of the CIMS due to energy non-accommodation (imperfect collisional thermalization). This is important for small molecules with less than 7-8 atoms (see **Article I** supplementary for details) as the cluster has too few vibrational modes to efficiently stabilize.

2. Fragmentation of thermalized clusters in the IMR region. If we consider that there are no barriers to the formation and evaporation processes, the rate of fragmentation should be relate to exp(-ΔG/RT), where ΔG is the formation free energy of the cluster, R is the gas constant and T is the temperature in Kelvin. The more negative the cluster formation free energy, the slower the fragmentation rate.

3. Non-thermal fragmentation due to energetic collisions with the bath gas molecules when accelerated in the first three chambers of the instrument. The extremely low pressures in the TOF region makes it unlikely that any collisions occur there.

If we consider that the fragmentation mechanism 2) dominates, the relative sensitivity of the instrument for a particular analyte X and reagent ion R^- can be given by:

$$\frac{d[X \cdot R^-]}{dt} = k_{coll} \cdot [X][R^-] - k_{frag}[X \cdot R^-], \tag{4.8}$$

where, k_{coll} is the analyte-ion collision rate, and k_{frag} is the thermal fragmentation rate of the cluster. Assuming that the analyte and ion concentrations

remain approximately constant inside the IMR region (i.e. only a small fraction is depleted by ion-molecule collisions), the expression can be integrated to obtain an equation for relative sensitivity (i.e. the relative fraction of [X]· $[R^-]$ to [X] at the end of the IMR region):

$$\frac{[X \cdot R^-]}{[X]} = \frac{k_{coll} \cdot [R^-]}{k_{frag}}(1 - exp(-k_{frag}\tau)), \tag{4.9}$$

where τ is the time the cluster is in the IMR region (generally in the order of 100 to 200 ms) and we assume the ion-molecule cluster concentration to be zero at $t = 0$. Two limiting cases can be identified: for sufficiently strong clusters, the fragmentation rate is close to zero, the clusters are detected at "maximum sensitivity", and we obtain (after a Taylor expansion of the exponential):

$$\frac{[X \cdot R^-]}{[X]} = k_{coll} \cdot [R^-]\tau. \tag{4.10}$$

The second limiting case is rapid thermal fragmentation of the cluster. In this case, a steady-state between the collision and fragmentation rates is obtained inside the IMR region:

$$\frac{[X \cdot R^-]}{[X]} = \frac{k_{coll}[R^-]}{k_{frag}}. \tag{4.11}$$

The collision rates between a neutral molecule and an ion can be computed using the parametrizations developed by Su and Bowers:[136]

$$\beta_{i,j} = \frac{q_i}{2\epsilon_0} m_{red}^{\frac{-1}{2}} [(4\pi\epsilon_0\alpha_j)^{\frac{1}{2}} + C\mu_j(\frac{2}{\pi k_B T})^{\frac{1}{2}}], \tag{4.12}$$

where, $\beta_{i,j} = k_{coll}$, q_i is the charge of the ion, ϵ_0 is the vacuum permittivity, m_{red} is the reduced mass of the two collision partners, and α_j and μ_j are polarizability and dipole moment of the neutral molecule, respectively. $C \in [0, 1]$ is an empirical factor scaling the importance of the ion-dipole term. In our calculations, C was given a value of 0.15, which was determined by Su and Bowers by a fit to experimental data. [136]

The only unknown factor in equation 4.11 is therefore the fragmentation rate k_{frag}. An estimation of k_{frag} can be obtained from elementary transition state theory (assuming no saddle points) and the equilibrium constant is the ratio between k_{coll} and k_{frag}.

$$k_{frag} = \frac{k_B T}{h} e^{\frac{-\Delta G}{RT}}, \tag{4.13}$$

where, k_B is the Boltzmann constant and h is the Planck constant. The equilibrium concentrations of the weakly bound (and therefore rapidly decomposing) molecule·reagent ion clusters can therefore be calculated using equation 4.11 and these should relate directly to their CIMS sensitivities. Whether this was observed to be the case is detailed in Chapter 5.

Results

5.1 Modeling CIMS sensitivities

In an iodide-CIMS, the I^--anion mostly forms one or more hydrogen bonds with the H-bond donating functional groups of the neutral sample molecule (see Figure 5.2). Molecules that offer two H-bond donating groups were found to cluster more strongly with the I^- anion than those with just one. While this was later shown to be a general pattern by the work of Hyttinen et al. [120], the work presented here sought to draw a comparison between the binding strength of the cluster and the sensitivity of one particular type of CIMS instrument. The sensitivities reported by Lee and Lopez-Hilifiker et al. [133] for their iodide-CIMS instrument (University of Washington CIMS, UW-CIMS) were used to make this comparison.

Cluster binding enthalpies were found to be reasonably good indicators of UW-CIMS sensitivities for a set of small atmospherically relevant carboxylic and dicarboxylic acids. The log-plot in Figure 5.1 shows the instrument sensitivities as a function of the calculated binding enthalpies for these molecules. From the molecules studied in **Article I**, those with the strongest binding enthalpies to I^- were dicarboxylic acids with 3 or more carbon atoms - malonic and succinic acids (see Figure 5.2 for the cluster geometries). Though a dicarboxylic acid, oxalic acid has a weak binding enthalpy to I^-. This is likely due to the more constrained hydrogen bonds between the two hydrogen atoms of the short 2-carbon oxalic acid and I^- relative to those of the longer chained dicarboxylic acids.

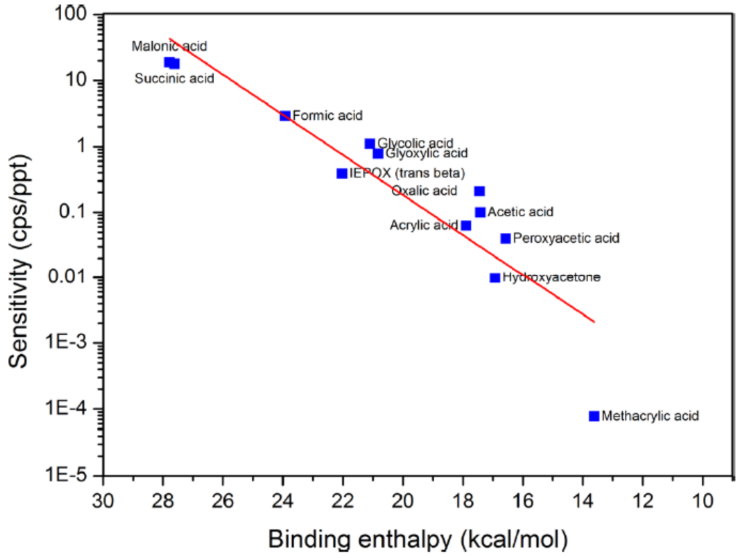

Figure 5.1: Comparison between the calculated binding enthalpies and CIMS sensitivities. The sensitivities are in units of counts per second (cps) per parts per trillion (ppt) concentration. Calculations were performed at the DLPNO-CCSD(T)/def2-QZVPP//PBE/aug-cc-pVTZ-PP level of theory.

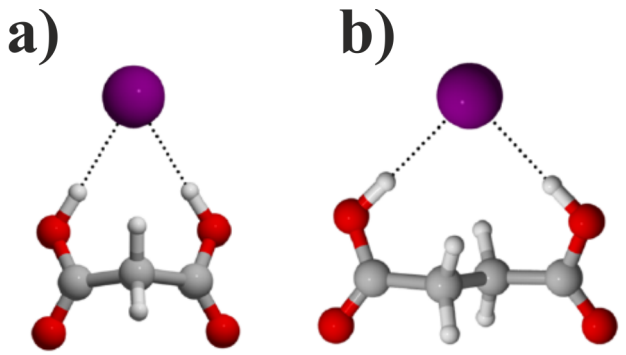

Figure 5.2: Lowest energy cluster geometries of a) malonic and b) succinic acids with iodide. Color coding: Grey - carbon, red - oxygen, white - hydrogen, purple - iodide.

The effective temperature that corresponds to cluster fragmentation

to give the empirical relationship shown in Figure 5.1 can be checked by expanding equation 4.13 into its entropic and enthalpic terms:

$$k_{frag} = \frac{k_B T}{h} e^{\frac{-\Delta G}{RT}} = \frac{k_B T}{h} e^{\frac{-(\Delta H - T\Delta S)}{RT}} = \frac{k_B T}{h} e^{\frac{\Delta S}{R}} e^{\frac{-\Delta H}{RT}}, \qquad (5.1)$$

where, ΔH and ΔS are the cluster formation enthalpy and entropy, respectively. Substituting k_{frag} in equation 4.11:

$$\frac{[X \cdot R^-]}{[X]} = \frac{k_{coll}[R^-]h}{k_B T} e^{\frac{-\Delta S}{R}} e^{\frac{\Delta H}{RT}} \qquad (5.2)$$

The term on the left-hand side of the above equation shows the fraction of molecule X clustered to the reagent ion and relates to the instrument sensitivity shown in Figure 5.1. Taking log on both sides (as log sensitivities were considered in Figure 5.1):

$$\log(\frac{[X \cdot R^-]}{[X]} = \log(\frac{k_{coll}[R^-]h}{k_B T} e^{\frac{-\Delta S}{R}}) + \frac{1}{RT}\Delta H. \qquad (5.3)$$

The first term on the right hand side in equation 5.3 can be considered a constant as the collision rate varied by less than a factor of 2 for the studied clusters and the entropy originates from a similar loss in rotational and translational degrees of freedom. The slope in Figure 5.1 may therefore be represented by $1/RT$. Using the obtained slope in **Article I** and solving for the temperature T results in T =∼1650 K. This shows that the fragmentation of the clusters is unlikely to be thermal as the temperature is completely unphysical in the context of a CIMS instrument. The fragmentation is therefore non-thermal and due to high-energy collisions of the clusters, likely in the ion guiding sections of the mass spectrometer where they are accelerated towards the detector. It was later shown that a model from first principles can predict non-thermal fragmentation inside a mass spectrometer that is in good agreement with experiments. [137]

One of the key results of **Article I** was that the log-linear plot depicting the iodide-CIMS sensitivities as a function of cluster binding enthalpies calculated at the low PBE/SDD level of theory showed a reasonable correlation between the two ($R^2 = 0.66$). Two outliers were found at this level, methacrylic acid and oxalic acid. Both molecules were found to have a stronger binding enthalpy to I^- than what their instrument sensitivities would indicate. For methacrylic acid, this is due to the fact that the log-linear relationship drawn in this article likely does not extend indefinitely - instead the instrument sensitivity as a function of the enthalpy is likely to

curve towards the axes at high and low binding enthalpies, with values that are specific to the UW-CIMS instrument. The cluster binding enthalpy of methacrylic acid with I^- approaches that of water·I^- (lower limit of the UW-CIMS detection sensitivity) and is therefore affected by the (probable) curving of the sensitivity - enthalpy relationship towards the x-axis. The binding enthalpy (and thus the predicted instrument sensitivity) of oxalic acid was found to depend strongly on the level of theory used in the computations. While the binding enthalpy of oxalic acid·I^- at the PBE/SDD level overestimated the sensitivity, the opposite was true at the higher DLPNO-CCSD(T)/def2-QZVPP//PBE/aug-cc-pVTZ-PP level of theory. This is because the single-point energy correction at the DLPNO-CCSD(T)/def2-QZVPP level of theory, which is performed on the lowest energy DFT cluster geometry, was likely not carried out on the actual lowest energy conformer. In other words, the conformational ordering following the DFT computations at the PBE/aug-cc-pVTZ-PP level of theory were inaccurate. DLPNO-CCSD(T) energy calculations on the different oxalic acid·I^- cluster conformers revealed an alternative minimum energy structure that was 8.4 kJ/mol lower in DLPNO-CCSD(T)-corrected binding enthalpy. By considering this cluster conformer, oxalic acid was no longer found to be an outlier.

Lee and Lopez-Hilfiker reported that the sensitivity of the UW-CIMS instrument for HONO and HNO_4 decreased with an increase in humidity, while the sensitivity increased HNO_3. [133] The effect of water on the clustering dynamics of these molecules with I^- was studied by looking at their binding enthalpies with $I{\cdot}H_2O^-$ ions as the I^- anion is more likely to be hydrated relative to the neutral molecules. The cluster binding enthalpies of the acids to $I{\cdot}H_2O^-$ was found to be lower by around 12.6 kJ/mol for HONO and HNO_4 and around 4.2 kJ/mol for HNO_3 relative to their binding enthalpies to the non-hydrated I^- anion. While the lower binding enthalpy would indicate a lowering of the instrument sensitivity for these molecules, the ligand-exchange reaction should favor the evaporation of the water molecule (since I^- clusters more strongly to HONO, HNO_3 and HNO_4 than to H_2O) stabilizing the cluster through sacrificial cooling, and thereby increasing the sensitivity of the UW-CIMS for these molecules. Our calculations would therefore indicate that the hydration of I^- by a single water molecule should have a net positive effect on the instrument sensitivities for all three molecules. The observed negative effect of humidity on HONO and HNO_4 sensitivities are likely due to factors unrelated to cluster binding enthalpies.

5.2 Detection of the HO_2 radical

The empirical relationship between instrument sensitivity and cluster binding enthalpy from **Article I** was used to predict the detection of the HO_2 radical by an iodide-CIMS instrument in **Article II**. The $HO_2 \cdot I^-$ cluster binding enthalpy was found to be 90.4 kJ/mol at the PBE/aug-cc-pVTZ-PP level and predicted to have an UW-CIMS sensitivity of around 0.40 cps ppt^{-1}. The HO_2 radical was subsequently successfully detected using an iodide-CIMS in a laboratory setting. The $HO_2 \cdot I^-$ cluster peak in the iodide-CIMS spectrum is shown in Figure 5.3 with the lowest energy cluster geometry in the inset.

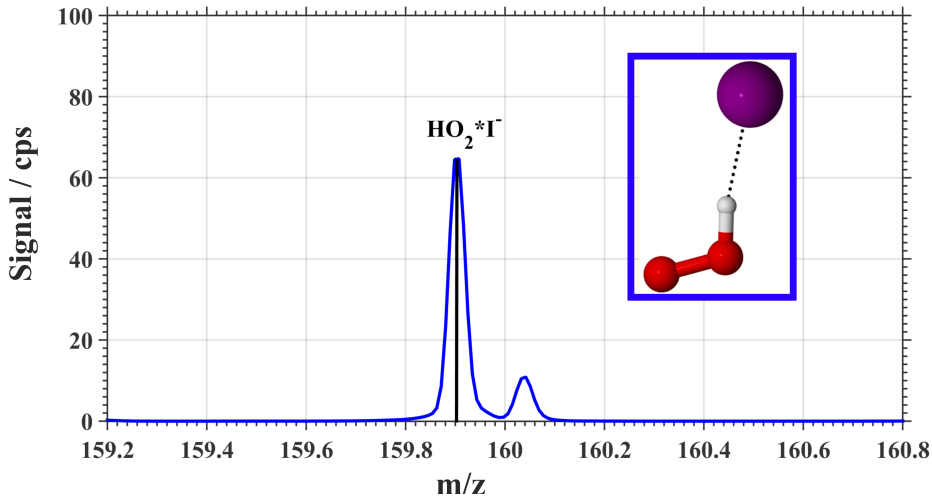

Figure 5.3: Peak corresponding to the $HO_2 \cdot I^-$ cluster in the iodide-CIMS spectrum. Inset: Lowest energy cluster geometry optimized at the PBE/aug-cc-pVTZ-PP level of theory. Color coding: Red - oxygen, white - hydrogen, purple - iodide.

The predicted sensitivity is close to the actual $HO_2 \cdot I^-$ sensitivity of 0.55 cps ppt^{-1} derived from the laboratory measurement (see **Article II** SI). The result is encouraging as a relatively low level calculation - without the DLPNO-CCSD(T) single point electronic energy correction for the $HO_2 \cdot I^-$ binding enthalpy in this case - resulted in a quite accurate prediction of the actual $HO_2 \cdot I^-$ sensitivity. It is important to note that the theoretical model is based on a different iodide-CIMS instrument (the UW-CIMS) and the predicted sensitivities therefore depend on the parameters of that instrument (such as the electric field strength of the transfer optics). It is

likely the case that a similar comparison between the predicted and actual iodide-CIMS (other than the UW-CIMS) sensitivities for an additional set of molecules will reveal a larger deviation than what was observed for the $HO_2 \cdot I^-$ case owing to the differences between the parameters of the particular iodide-CIMS instrument used and the UW-CIMS. However, the method is unlikely to result in false negatives, especially for the "maximum sensitivity" molecules (i.e. molecules with strong binding enthalpies in the maximum sensitivity range are very likely to be detected by an iodide-CIMS).

The proclivity of the I^- anion to be hydrated in the iodide-CIMS IMR has been described in Chapter 4. The humidity dependence of the iodide-CIMS method is therefore important to consider. In **Article II**, we found that the $HO_2 \cdot I^-$ signal showed a strong negative dependence to humidity. A similarly strong negative humidity dependence was observed by Albrecht et al. [138] in their HO_2 radical detection using a Br-CIMS. This is expected as the Br^- anion is similarly susceptible to hydration (as discussed in Chapter 4). Note that the ionization in the iodide-CIMS used in **Article II** was carried out at 1 atm (atmospheric) pressure, while the Br-CIMS study by Albrecht et al. used low pressure ionization. This likely affects how hydrated the reagent ion is inside the IMR. A lower degree of hydration of reagent ions can be expected in low pressure ionization due to the water molecules likely evaporating from lack of stabilization from collisions with gas molecules, while the opposite is the case in atmospheric pressure ionization.

5.3 Detection of VOC oxidation products by I^- and Br^- and comparing CIMS methods

In addition to the detection of the HO_2 radical, the potential of the iodide-CIMS to detect the oxidation products of VOCs, specifically cyclohexene, was investigated in **Article II**. This was the first time an iodide-CIMS was used to try to detect the higher oxidized products of VOC oxidation. As was done with the HO_2 radical, the binding enthalpies of some of the cyclohexene oxidation products with I^- were computed. Figure 5.4 shows the optimized cluster geometries of the computed molecules.

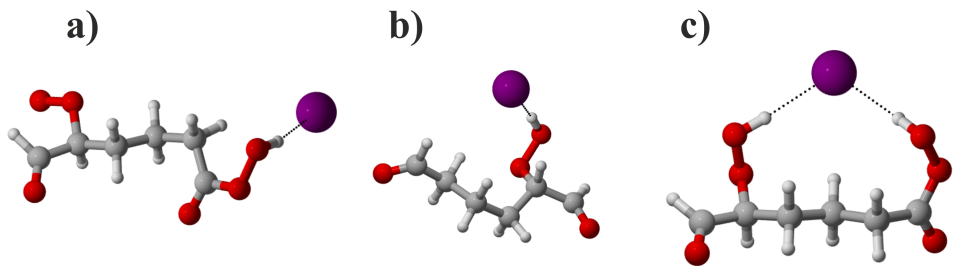

Figure 5.4: Optimized geometries of cyclohexene ozonolysis derived $RO_2 \cdot I^-$ a) $C_6H_9O_6 \cdot I^-$ and closed-shell product$\cdot I^-$ b) $C_6H_{10}O_4 \cdot I^-$, c) $C_6H_{10}O_6 \cdot I^-$. Color coding: Grey - carbon, red - oxygen, white - hydrogen, purple - iodide.

The $C_6H_{10}O_6 \cdot I^-$ cluster was the most strongly bound at 102.2 kJ/mol, but all three molecules had predicted sensitivities between 1 to 4 cps ppt^{-1} (around that of glyoxylic acid, glycolic acid and formic acid in Figure 5.1).

In addition, the efficiencies of iodide-CIMS and bromide-CIMS in detecting the oxidation products of VOCs were compared to that of the nitrate-CIMS in **Article II** and **Article V**, respectively. As discussed in Chapter 4, NO_3^- is a highly selective towards the higher oxidized molecules (oxygen:carbon,O:C ratio 1 to 1.5). This was found to be the case for the oxidation products of both cyclohexene and α-pinene. I^- and Br^- were found to be adept at detecting the lower oxidized (0.5 to 0.66). Interestingly, iodide-CIMS was also quite good at detecting the higher oxidized species from cyclohexene oxidation (matching that of nitrate-CIMS).

It is important to note here that because the nitrate-CIMS is so selective, the spectra is a lot less noisy than that of the iodide- or bromide-CIMS. This makes the peak composition analysis much simpler.

One of the more important computational result of **Article II** was establishing the mechanisms of the dehydroxylation and deoxygenation reactions of peroxy acids and acetyl peroxy radicals in an iodide-CIMS instrument. Hydrated I^- anions were found to abstract an OH (dehydroxylate) from peroxy acids and an O (deoxygenate) from an acetyl peroxy radical, converting them both to carboxylate anions. Some of these molecules are therefore detected as carboxylate anions by the iodide-CIMS instrument and this should be taken into account when considering sample concentrations.

5.4 Thermodynamics and kinetics of gas-phase peroxy radical reactions

The gas-phase chemistry of RO_2 radicals was investigated experimentally in **Article II**. In **Article III** and **Article IV**, this chemistry was probed in greater detail using purely computational methods. The radical recycling reactions $RO_2 + HO_2 \rightarrow RO + OH + O_2$ and $RO_2 + R^{'}O_2 \rightarrow RO + R^{'}O + O_2$ were investigated for first-generation peroxy radicals derived from the oxidation of select monoterpenes in **Article III**. The reaction Gibbs energies were less than 0 for both reactions for all of the studied systems (indicating that the reaction is thermodynamically favorable). The reactions were more exothermic for RO_2 derived from O_3 oxidation than those from OH and NO_3 oxidation, indicating that these reactions are likely more important for the O_3 oxidized systems.

The primary result of **Article III** is that $RO_2 + HO_2$ and RO_2 and $R^{'}O_2$ reactions for monoterpene-derived first-generation peroxy radicals can lead to radical products in the atmosphere. The alkoxy radical products can continue to undergo reactions that could potentially lead additional HOM formation. The generation of the OH radical as a product helps recycle the oxidant, increasing the oxidative capacity of the immediate atmosphere.

While the transition states for the two studied reactions were not computed for the monoterpene-derived first-generation peroxy radicals, some general mechanistic assumption were made based on the entropy penalties to the transition state and intermediate complexes relative to the separated products to deduce the atmospheric relevance of these reactions. Figure 5.5 shows the stationary points of the studied $RO_2 + HO_2$ reaction for a model OH-oxidized RO_2 $CH_2(OH)CH_2OO$ in terms of enthalpy, entropy contribution to Gibbs energy, at 298.15 K, and Gibbs energy. This temperature is a relevant atmospheric temperature where these reactions occur. The parameters can be re-calculated for a different temperature by using equation 3.21. From the reaction Gibbs energy, an estimation of the Gibbs energy of the TS can be made from the entropy contribution to the Gibbs energy of the TS relative to the products (around 84 kJ/mol above the products) and the lowering of the TS enthalpy due to an intra-molecular H-bond in the TS complex (around 42 kJ/mol). The mechanistic assumptions made are described in detail in **Article III**.

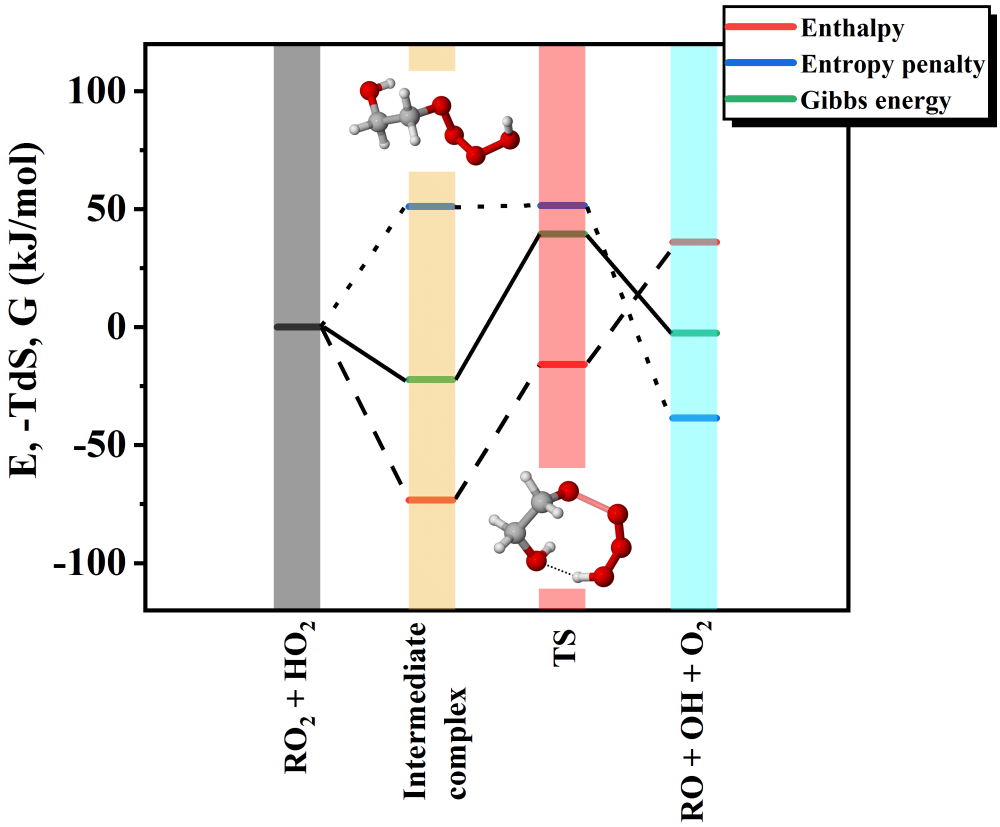

Figure 5.5: Reaction stationary points for the RO_2 + HO_2 for a model system oxidized via OH addition. Only the rate limiting TS is shown and the intermediate and TS complexes between that and the products are not shown. The energetics are shown in terms of enthalpy (red lines), entropy contribution to Gibbs energies (-TΔS at T = 298.15 K; blue lines), and Gibbs energies (green lines). Also shown is the lowest energy intermediate and TS complex geometries. Molecule color coding: Grey - carbon, red - oxygen, white - hydrogen.

5.5 Kinetics of RO_2 + RO reaction on the singlet surface

In **Article IV**, the kinetics of the peroxy radical reactions with OH and alkoxy radicals were investigated computationally. For the RO_2 + OH reaction, non-alkyl carbonyl-containing β-oxo and acetyl type RO_2s were

considered (since similar studies on alkyl-type RO_2 have been carried out previously). While the results for the β-oxo system were similar to those of the alkyl systems, i.e., the formation of an ROOOH adduct and RO + HO_2 as its most likely breakup channel, the likely product channel for the acetyl system is the formation of acetic acid and a singlet O_2. The stationary points of the RO_2 + OH reaction for the β-oxo and acetyl RO_2s are shown in Figure 5.6.

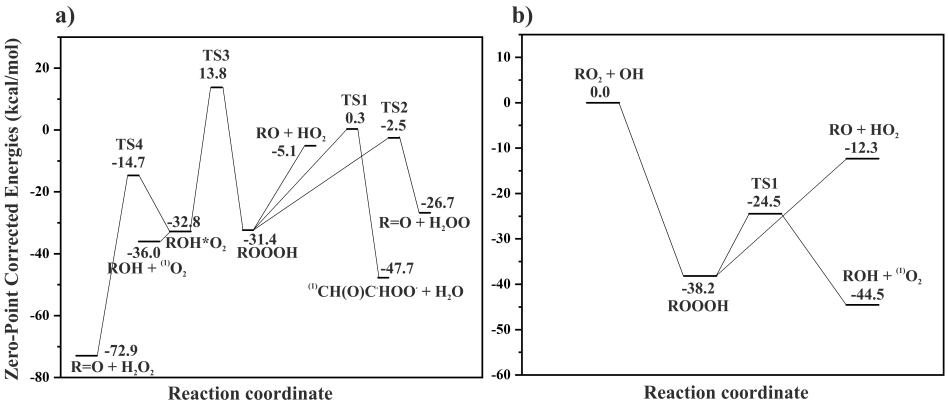

Figure 5.6: Stationary points of the RO_2 + OH reaction for a) β-oxo-type RO_2 CH(O)CH2OO and b) acetyl-type $CH_3C(O)OO$ on the singlet surface calculated at the ROHF-ROCCSD(T)-F12a/VDZ-F12//ωB97X-D/aug-cc-pVTZ level. The energetics of the β-oxo case are relative to the reactants RO_2 + OH (not shown). Note: ROH in b) is not an alcohol but a carboxylic acid.

The $R'O_2$ + RO reaction was computed for 2-carbon model alkyl, β-oxo and acetyl peroxy and alkoxy systems in **Article IV** and were found to form an R′OOOR trioxide adduct. The $R'O_2$ + RO association reaction was found to be barrierless following a relaxed scan over the $R'OO\cdots OR$ bond length of the optimized adduct at the UωB97X-D/6-31+G* level of theory. Once formed, the R′OOOR adduct can decompose back to the reactants $R'O_2$ + RO (or to RO_2 + R′O), form a Criegee intermediate ($R^{\cdot}_{\_H}OO^{\cdot}$) and an alcohol or carboxylic acid (ROH/R(O)OH), or form a hydroperoxide (ROOH) and a carbonyl compound (R=O). The most likely decomposition pathway of R′OOOR was found to be back into $R'O_2$ + RO (or RO_2 + R′O) for all studied systems. The lifetimes of these adducts were calculated by incorporating the computed thermochemical data into the master equation solver for multi energy well reactions (MESMER) program.

The collisional stabilization of the R′OOOR adducts were calculated using the collisional energy transfer E_{down} model for N_2 bath gas.

The lifetimes of these adducts differed significantly for the different reacting radical structures. The adducts formed following the R′O_2 + RO reaction where one of the reactant radicals was of the acetyl type were found to have a significantly shorter lifetime (0.01 - 0.1 seconds) in comparison to non-acetyl containing systems (or when both reacting radicals were of the acetyl type). This is due the resonance stabilization between the two oxygen atoms of the nascent acetyl alkoxy radical, lowering this product channel energy substantially.

The longest R′OOOR adduct lifetime corresponded to the β-oxo-β-oxo system (100 seconds).

Conclusions

6.1 Article I: Cluster binding enthalpies and iodide-CIMS sensitivities

The iodide-CIMS has been used to detect small organic and inorganic acids, and halogen species. In **Article I**, molecule·I^- cluster binding enthalpies were calculated and then compared to the reported UW-CIMS instrument sensitivities for a set of these molecules. A log-linear plot was drawn, which showed a reasonable correlation between the calculated binding strength of the clusters and the reported instrument sensitivities. Such a plot is a useful tool when speculating whether a certain molecule will be detected by a specific CIMS method.

One of the key results of this article was that low-level computational calculations (and therefore rapid and computationally inexpensive) were able to provide a good correlation between cluster binding enthalpies and iodide-CIMS sensitivities. The use of the higher DLPNO-CCSD(T)/def2-QZVPP//PBE/aug-cc-pVTZ-PP level of theory was found to improve the correlation further. However, there were outliers, such as the "maximum sensitivity" molecules. These molecules were detected at the maximum possible sensitivity of the iodide-CIMS and were only constrained by the collision frequencies of the sample molecules and I^- anions in the IMR of the instrument. Our calculations underpredicted the binding enthalpies of these compounds to I^- and this method can therefore give false negatives, or molecules that are found to bind weakly to I^- from the quantum chemical calculations, but are actually detected at maximum sensitivities. Examples of such outliers were methylerythritol and levoglucosan. However, our data set contained only one false positive, i.e. an over prediction of the binding enthalpy relative to the detected sensitivity, at the low PBE/SDD level of theory and no false positives at the higher DLPNO-CCSD(T)/def2-QZVPP//PBE/aug-cc-pVTZ-PP level of theory.

While the binding enthalpy vs UW-CIMS sensitivities gave a reasonable correlation, the fragmentation of the molecule·I^- clusters are likely non-thermal and due to their energetic collisions with bath-gas molecules inside the mass spectrometer. This model can be significantly improved by considering the non-thermal fragmentation rates using models developed by for example Zapadinsky et al. [139]

6.2 Article II: Theoretical and experimental study of the detection of HO_2 radical and the products of cyclohexene ozonolysis using iodide-CIMS

The theoretical study in **Article I** on the efficiency of iodide-CIMS to detect a set of small carboxylic and inorganic acids was followed by investigating the efficiency of this method to detect the HO_2 radical and the oxidation products of cyclohexene. Computational calculations on the molecule·I^- cluster binding enthalpies helped predict the detectibility of these molecules by an iodide-CIMS before their actual detection in a laboratory setting.

The experimental comparison between the nitrate- and iodide-CIMS methods showed the iodide-CIMS is able to pick up the lower-oxidized products more efficiently than nitrate-CIMS. The higher-oxidized molecules were detected similarly well by both methods. One draw back of the iodide-CIMS method is that its low-selectivity makes the analysis of its spectra difficult; the spectra is more noisy compared to the nitrate-CIMS.

6.3 Article III: Thermodynamics of RO_2 + HO_2 and RO_2 + RO_2 reactions that lead to radical recycling

The study of the gas-phase chemistry of RO_2 radicals was continued in **Article III** but a switch to a pure theoretical study was made. The thermodynamics of two important RO_2 bimolecular reactions in the atmosphere that can lead to radical recycling; RO_2 + HO_2 and RO_2 + RO_2 were investigated. The molecules that were studied were OH, NO_3 and O_3 oxidized first-generation RO_2 products of α-pinene, β-pinene, limonene, trans-β-ocimene and Δ^3-carene. The results indicated that these radical recycling

product channels are likely most important for the O_3 oxidized systems, and especially so for β-pinene. The recycling of radical species likely contribute measurably to SOA formation by not terminating the processes that lead to the formation of low volatile compounds.

6.4 Article IV: Mechanism to form stable adducts from gas-phase reactions of alkoxy and peroxy radicals

Article IV continued the theoretical investigation into the gas-phase reactions of RO_2 by looking at other bimolecular reaction partners, namely OH and RO. The mechanism for the reaction between RO_2 + OH for model "Rs" of types β-oxo $CH(O)CH_2$ and acetyl $CH_3C(O)OO$, and for the reaction between RO_2 + RO for the model "R" of type alkyl CH_3CH_2 in addition to the previous two showed that both reactions go through a trioxide adduct; ROOOH and ROOOR, respectively.

In the first reaction, the ROOOH adduct corresponding to the β-oxo system will likely decompose into the products RO and HO_2, while that corresponding to the acetyl system will likely decompose into the products R(O)OH and O_2. For the $R^{'}O_2$ + RO reactions, the $R^{'}OOOR$ adducts were most likely to decompose back into $R^{'}O_2$ + RO (RO_2 + $R^{'}O$), with the systems that contained one acetyl radical decomposing the fastest (i.e. β-oxo-acetyl - $CH(O)CH_2OOOC(O)CH_3$ and alkyl-acetyl - $CH_3CH_2OOOC(O)CH_3$), with a lifetime of $\sim$0.01 seconds. The β-oxo-β-oxo system was found to have the longest lifetime of 100 seconds. Some of these molecules can therefore have significant lifetimes and, if sufficiently involatile, can directly play a role in SOA formation in the form of condensing vapors.

6.5 Article V: Rapid switching between reagent ions and the detection of VOC oxidation products

The purely experimental **Article V** followed up on the reagent ion comparison carried out in **Article II** with a sophisticated new MION inlet system capable of rapid switching between reagent ions. Two reagent ions, Br^- and NO_3^- were used concomitantly to detect the oxidation products of cyclohexene and α-pinene. This study was a step up from the previous one as it was possible to keep the experimental conditions exactly the same

for the two reagent ions. This allowed for a direct comparison between the two spectra. The MION inlet is a powerful tool that allows the probing of important gas-phase chemistry.

References

[1] Schulze, E. D.; Luyssaert, P.; Ciais, P.; Freibauer, A.; Janssens, I. A.; Soussana, J. F.; Smith, P.; Grace, J.; Levin, I.; Thiruchittampalam, B.; et al. Importance of Methane and Nitrous Oxide for Europe's Terrestrial Greenhouse-Gas Balance. *Nat. Geo.* **2009**, *2*, 842-850.

[2] Howarth, R. W. A Bridge to Nowhere: Methane Emissions and the Greenhouse Gas Footprint of Natural Gas. *En. Sci. Eng.* **2014**, *2*, 47-60.

[3] Philipona, R.; Dürr, Ohmura, A.; Ruckstuhl, C. Anthropogenic Greenhouse Forcing and Strong Water Vapor Feedback Increase Temperature in Europe. *Geo. Phys. Lett.* **2005**, *32*, L19809.

[4] Solomon, S.; Rosenlof, K. H.; Portmann, R. W.; Daniel, J. S.; Davis, S. M.; Sanford, T. J.; Plattner, G. Contribution of Stratospheric Water Vapor to Decadal Changes in the Rate of Global Warming. *Sci.* **2010**, *327*, 1219-1223.

[5] Pankow, J. F. An Adsorption Model of the Gas/Aerosol Partitioning Involved in the Formation of Secondary Organic Aerosol. *Atmos. Environ.* **1994**, *28*, 189-193.

[6] Odum, J. R.; Hoffmann, T.; Bowman, F.; Collins, D.; Flagan, R. C.; Seinfeld, J. H. Gas/Particle Partitioning and Secondary Organic Aerosol Yields. *Environ. Sci. Tech.* **1996**, *30*, 2580-2585.

[7] Sindelarova, K.; Granier, C.; Bouarar, I.; Guenther, A.; Tilmes, S.; Stavrakou, T.; Müller, J. -F.; Kuhn, U.; Stefani, P.; Knorr, W. Global Data Set of Biogenic VOC Emissions Calculated by the MEGAN Model Over the Last 30 Years. *Atmos. Chem. Phys.* **2014**, *14*, 9317-9341.

[8] Guenther, A.; Hewitt, C. N.; Erickson, D.; Fall, R.; Geron, C.; Graedel, T.; Harley, P.; Klinger, L.; Lerdau, M.; McKay, W. A.; et al. A Global

Model of Natural Volatile Organic Compound Emissions. *J. Geophys. Res.* **1995**, *100*, 8873-8892.

[9] Guenther, A.; Hewitt, C. N.; Erickson, D.; Fall, R.; Geron, C.; Graedel, T.; Harley, P.; Klinger, L.; Lerdau, M.; McKay, W. A.; Pierce, T.; Scholes, B.; Steinbrecher, R.; Tallamraju, R.; Taylor, J.; Zimmerman, P. A Global Model of Natural Volatile Organic Compound Emissions. *J. Geophys. Res.* **1995**, *100*, 8873-8892.

[10] Guenther, A.; Geron, C.; Pierce, T.; Lamb, B.; Harley, P.; Fall, R. Natural Emissions of Non-Methane Volatile Organic Compounds, Carbon Monoxide, and Oxides of Nitrogen from North America. *Atmos. Env.* **2000**, *34*, 2205-2230.

[11] Fall, R. Biogenic Emissions of Volatile Organic Compounds from Higher Plants. *Reactive Hydrocarbons in the Atmosphere* **1999**, 41-96.

[12] Fuentes, J. D.; Lerdau, M.; Atkinson, R.; Baldocchi, D.; Bottenheim, J. W.; Cicciolo, P.; Lamp, B.; Geron, C.; Gu, L.; Guenther, A.; Sharkey, T. D.; Stockwell, W. Biogenic Hydrocarbons in the Atmospheric Boundary Layer: A Review. *Bull. Amer. Meteor. Soc.* **2000**, *81*, 1537-1576.

[13] Atkinson, R.; Arey, J. Gas-Phase Tropospheric Chemistry of Biogenic Volatile Organic Compounds: A Review. *Atmos. Env.* **2003**, *37*, 197-219.

[14] Granier, C.; Pétron, G.; Müller, J. -F.; Brasseur, G. The Impact of Natural and Anthropogenic Hydrocarbons on the Tropospheric Budget of Carbon Monoxide. Atmos. Environ. 2000, 34, 5255-5270.

[15] Poisson, N.; Kanakidou, M.; Crutzen, P. J. Impact of Non-Methane Hydrocarbons on Tropospheric Chemistry and the Oxidizing Power of the Global Troposphere: 3-Dimensional Modelling Results. *J. Atmos. Chem.* **2000**, *36*, 157-230.

[16] Pfister, G.; Emmons, L.; Hess, P.; Lamarque, J. -F.; Orlando, J.; Walters, S.; Guenther, A.; Palmer, P.; and Lawrence, P. Contribution of Isoprene to Chemical Budgets: A Model Tracer Study with the NCAR CTM MOZART-4. *J. Geophys. Res.* **2008**, *113*, D05308.

[17] Berndt, T.; Richters, S.; Kaethner, R.; Voigtländer, J.; Stratmann, F.; Sipilä, M.; Kulmala, M.; Herrmann, H. Gas-Phase Ozonolysis of Cycloalkenes: Formation of Highly Oxidized RO_2 Radicals and Their

Reactions with NO, NO_2, SO_2, and Other RO_2 Radicals. *J. Phys. Chem. A* **2015**, *119*, 10336-10348.

[18] Ehn, M.; Thornton, J. A.; Kleist, E.; Sipilä, M.; Junninen, H.; Pullinen, I.; Springer, M.; Rubach, F.; Tillmann, R.; Lee, B.; et al. A Large Source of Low-Volatility Secondary Organic Aerosol. *Nature* **2014**, *506*, 476-479.

[19] Rissanen, M. P.; Kurtén, T.; Sipilä, M.; Thornton, J. A.; Kausiala, O.; Garmash, O.; Kjaergaard, H. G.; Petäjä, T.; Worsnop, D. R.; Ehn, M.; Kulmala, M. Effects of Chemical Complexity on the Autoxidation Mechanisms of Endocyclic Alkene Ozonolysis Products: From Methylcyclohexenes Toward Understanding α-Pinene. *J. Phys. Chem. A* **2015**, *119*, 4633-4650.

[20] Rissanen, M. P.; Kurtén, T.; Sipilä, M.; Thornton, J. A.; Kangasluoma, J.; Sarnela, N.; Junninen, H.; Jørgensen, S.; Schallhart, S.; Kajos, M. K.; et al. The Formation of Highly Oxidized Multifunctional Products in the Ozonolysis of Cyclohexene. *J. Am. Chem. Soc.* **2014**, *136*, 15596-15606.

[21] Lelieveld, J.; Butler, T. M.; Crowley, J. N.; Dillon, T. J.; Fischer, H.; Ganzeveld, L.; Harder, H.; Lawrence, M. G.; Martinez, M.; Taraborrelli, D.; Williams, J. Atmopsheric Oxidation Capacity Sustained by a Tropical Forest. *Nature* **2008**, *452*, 737-740.

[22] Sheehy, P. M.; Volkamer, R.; Molina, M. J. Oxidative Capacity of the Mexico City Atmosphere - Part 2: A RO_x Radical Cycling Perspective. *Atmos. Chem. Phys.* **2010**, *10*, 6993-7008.

[23] Dash, M. R.; Rajakumar, B. Experimental and Theoretical Rate Coefficients for the Gas Phase Reaction of β-Pinene with OH Radical. *Atmos. Env.* **2013**, *79*, 161-171.

[24] Sato, K.; Nakashima, Y.; Morino, Y.; Imamura, T.; Kurokawa, J.; Kajii, Y. Total OH Reactivity Measurements for the OH-Initiated Oxidation of Aromatic Hydrocarbons in the Presence of NO_x. *Atmos. Environ.* **2017**, *171*, 272-278.

[25] Su, H.; Cheng, Y.; Oswald, R.; Behrendt, T.; Trebs, I.; Meixner, F. X.; Andreae, M. O.; Cheng, P.; Zhang, Y.; Pöschl, U. Soil Nitrate as a Source of Atmospheric HONO and OH Radicals. *Sci.* **2011**, *333*, 1616-1618.

[26] Loison, J.-C.; Daranlot, J.; Bergeat, A.; Caralp, F.; Mereau, R.; Hickson, K. M. Gas-Phase Kinetics of Hydroxyl Radical Reactions with C_3H_6 and C_4H_8: Product Branching Ratios and OH Addition Site-Specificity. *J. Phys. Chem. A* **2010**, *114*, 13326-13336.

[27] Atkinson, R. Kinetics and Mechanisms of the Gas-Phase Reactions of the Hydroxyl Radical with Organic Compounds under Atmospheric Conditions. *Chem. Rev.* **1985**, *85*, 69-201.

[28] Allan, B. J.; McFiggans, G.; Plane, J. M. C. The Nitrate Radical in the Remote Marine Boundary Layer. J. Geophys. Res. **2000**, *105*, 24191-24204.

[29] Atkinson, R.; Baulch, D. L.; Cox, R. A.; Hampson, R. F.; Kerr, J. A.; Troe, J. Evaluated Kinetic and Photochemical Data for Atmospheric Chemistry: Supplement III. IUPAC Subcommittee on Gas Kinetics Data Evaluation for Atmospheric Chemistry. *J. Phys. Chem. Ref. Dat.* **1989**, *18*, 881.

[30] Geyer, A.; Alicke, B.; Ackermann, R.; Martinez, M.; Harder, H.; Brune, W.; di Carlo, P.; Williams, E.; Jobson, T.; Hall, S.; Shetter, R.; Stutz, J. Direct Observations of Daytime NO_3: Implications for Urban Boundary Layer Chemistry. *J. Geophys. Res.* **2003**, *108*, 4368.

[31] Ayres, B. R.; Allen, H. M.; Draper, D. C.; Brown, S. S.; Wild, R. J.; Jimenez, J. L.; Day, D. A.; Campuzano-Jost, P.; Hu, W.; de Gouw, J.; et al. Organic Nitrate Aerosol Formation via NO_3 + Biogenic Volatile Organic Compounds in the Southeastern United States. *Atmos. Chem. Phys.* **2015**, *15*, 13377-13392.

[32] Martínez, E.; Cabañas, B.; Aranda, A.; Martín, P.; Salgado, S. Absolute Rate Coefficients for the Gas-Phase Reactions of NO_3 Radical with a Series of Monoterpenes at T = 298 to 433 K. *J. Atmos. Chem.* **1999**, *33*, 265-282.

[33] Atkinson, R. Kinetics and Mechanisms of the Gas-Phase Reactions of the NO_3 Radical with Organic Compounds. *J. Phys. Chem. Ref. Data* **1991**, *20*, 459-507.

[34] Tarasick, D. W.; Carey-Smith, T. K.; Hocking, W. K.; Moeini, O.; He, H.; Liu, J.; Osman, M. K.; Thompson, A. M.; Johnson, B. J.; Oltmans, S. J.; Merrill, J. T. Quantifying Stratosphere-Troposphere Transport of Ozone Using Balloon-Borne Ozonesondes, Radar Windprofilers and Trajectory Models. *Atmos. Environ.* **2019**, *198*, 496-509.

[35] Lelieveld, J.; van Aardenne, J.; Fischer, H.; de Reus, M.; Williams, J.; Winkler, P. Increasing Ozone over the Atlantic Ocean. *Sci.* **2004**, *304*, 1483-1487.

[36] Kourtchev, I.; Ruuskanen, T. M.; Keronen, P.; Sogacheva, L.; Del Maso, M.; Reissell, A.; Chi, X.; Vermeylen, R.; Kulmala, M.; Maenhaut, W.; Claeys, M. Determination of Isoprene and α-/β-Pinene Oxidation Products in Boreal Forest Aerosols from Hyytiälä, Finland: Diel Variations and Possible Link with Particle Formation Events. *Atmos. Environ.* **1994**, *28*, 53-68.

[37] Khamaganov, V. G.; Hites, R. A. Rate Constants for the Gas-Phase Reactions of Ozone with Isoprene, α- and β-Pinene, and Limonene as a Function of Temperature. *J. Phys. Chem. A* **2001**, *105*, 815-822.

[38] Kim, D.; Stevens, P. S.; Hites, R. A. Rate Constants for the Gas-Phase Reactions of OH and O_3 with β-Ocimene, β-Myrcene, and α- and β-Farnesene as a Function of Temperature. *J. Phys. Chem. A* **2011**, *115*, 500-506.

[39] Long, B.; Bao, J. L.; and Truhlar, D. G. Atmospheric Chemistry of Criegee Intermediates: Unimolecular Reactions and Reactions with Water. *J. Am. Chem. Soc.* **2016**, *138*, 14409-14422.

[40] Johnson D.; Marston, G. The Gas-Phase Ozonolysis of Unsaturated Volatile Organic Compounds in the Troposphere. *Chem. Soc. Rev.* **2008**, *37*, 699-716.

[41] Vereecken, L. Lifting the Veil on an Old Mystery. *Science* **2013**, *340*, 154-155.

[42] Taatjes, C. A.; Shallcross, D. E.; Percival, C. Research Frontiers in the Chemistry of Criegee Intermediates and Tropospheric Ozonolysis. *Phys. Chem. Chem. Phys.* **2014**, *16*, 1704-1718.

[43] Atkinson, R.; Arey, J. Gas-Phase Tropospheric Chemistry of Biogenic Volatile Organic Compounds: A Review. *Atmos. Env.* **2003**, *37*, 197-219.

[44] Jenkin, M. E.; Valorso, R.; Aumont, B.; Rickard, A. R. Estimation of Rate Coefficients and Branching Ratios for Reactions of Organic Peroxy Radicals for use in Automated Mechanism Construction. *Atmos. Chem. Phys.* **2019**, *19*, 7691-7717.

[45] Archibald, A. T.; Petit, A. S.; Percival, C. J.; Harvey, J. N.; Shallcross, D. E. On the Importance of the Reaction Between OH and RO_2 Radicals. *Atmos. Sci. Lett.* **2009**, *10*, 102-108.

[46] Müller, J-. F.; Liu, Z.; Nguyen, V. S.; Stavrakou, T.; Harvey, J. N.; Peeters, J. The Reaction of Methyl Peroxy and Hydroxyl Radicals as a Major Source of Atmospheric Methanol. *Nat. Comm.* **2016**, *7*, 13213.

[47] Assaf, E.; Schoemaecker, C.; Vereecken, L.; Fittschen, C. Experimental and Theoretical Investigation of the Reaction of RO_2 Radicals with OH Radicals: Dependence of the HO_2 Yield on the Size of the Alkyl Group. *Int. J. Chem. Kinet.* **2018**, *50*, 1-11.

[48] Fittschen, C.; Ajami, M. A.; Batut, S.; Ferracci, V.; Archer-Nicholls, S.; Archibald, A. T. Schoemaecker, C. ROOOH: A Missing Piece of the Puzzle for OH Measurements in Low-NO Environments. *Atmos. Chem. Phys.* **2019**, *19*, 349-362.

[49] Wolfe, G. M.; Cantrell, C.; Kim, S.; Mauldin III, R. L.; Karl, T.; Harley, P.; Turnipseed, A.; Zheng, W.; Flocke, F.; Apel, E. C.; et al. Missing Peroxy Radical Sources within a Summertime Ponderosa Pine Forest. *Atmos. Chem. Phys.* **2014**, *14*, 4715-4732.

[50] Lu, X.; Chen, N.; Wang, Y.; Cao, W.; Zhu, B.; Yao, T.; Fung, J. C. H.; lau, A. K. H. Radical Budget and Ozone Chemistry During Autumn in the Atmosphere of an Urban Site in Central China. *J. Geophys. Res. Atmos.* **2016**, *122*, 3672-3685.

[51] Benson, S. W.; Nangia, P. S. Some Unresolved Problems in Oxidation and Combustion. *Acc. Chem. Res.* **1979**, *12*, 223-228.

[52] Benson, S. W. The Kinetics and Thermochemistry of Chemical Oxidation with Application to Combustion and Flames. *Prog. Energy Combust. Sci.* **1981**, *7*, 125-134.

[53] Nangia, P. S.; Benson, S. W. Thermochemistry and Kinetics of Ozonation Reactions. *J. Am. Chem. Soc.* **1980**, *102*, 3105-3115.

[54] Winiberg, F. A. F.; Dillon, T. J.; Orr, S. C.; Groß, C. B. M.; Bejan, I.; Brumby, C. A.; Evans, M. J.; Smith, S. C.; Heard, D. E.; and Seakins, P. W. Direct Measurements of OH and Other Product Yields from the HO_2 + $CH_3C(O)O_2$ Reaction. *Atmos. Chem. Phys.* **2016**, *16*, 4023-4042.

[55] Hasson, A. S.; Tyndall, G. S.; Orlando, J. J.; Singh, S.; Hernandez, S. Q.; Cambell, S.; and Ibarra, Y. Branching Ratios For the Reaction of Selected Carbonyl-Containing Peroxy Radicals With Hydroperoxy Radicals. *J. Phys. Chem. A* **2012**, *116*, 6264-6281.

[56] Hasson, A. S.; Tyndall, G. S.; and Orlando, J. J. A Product Yield Study of the Reaction of HO_2 Radicals with Ethyl Peroxy ($C_2H_5O_2$), Acetyl Peroxy ($CH_3C(O)O_2$), and Acetonyl Peroxy ($CH_3C(O)CH_2O_2$) Radicals. *J. Phys. Chem. A* **2004**, *108*, 5979-5989.

[57] Hasson, A. S.; Kuwata, K. T.; Arroyo, M. C.; Petersen, E. B. Theoretical Studies of the Reaction of Hydroperoxy Radicals (HO_2) With Ethyl Peroxy ($CH_3CH_2O_2$), Acetyl Peroxy ($CH_3C(O)O_2$), and Acetonyl Peroxy ($CH_3C(O)CH_2O_2$) Radicals. *J. Photochem. Photobiol. A* **2005**, *176*, 218-230.

[58] Xu, L.; Møller, K. H.; Crounse, J. D.; Otkjær, R. V.; Kjaergaard, H. G.; Wennberg, P. O. Unimolecular Reactions of Peroxy Radicals Formed in the Oxidation of α-Pinene and β-Pinene by Hydroxyl Radicals. *J. Phys. Chem. A* **2019**, *123*, 1661-1674.

[59] Teng, A. P.; Crounse, J. D.; Wennberg, P. O. Isoprene Peroxy Radical Dynamics. *J. Am. Chem. Soc.* **2017**, *139*, 5367-5377.

[60] Praske, E.; Otkjær, R. V.; Crounse, J. D.; Hethcox, J. C.; Stoltz, B. M.; Kjaergaard, H. G.; Wennberg, P. O. Atmospheric Autoxidation Is Increasingly Important in Urban and Suburban North America. *Proc. Natl. Acad. Sci. U. S. A.* **2018**, *115*, 64-69.

[61] Crounse, J. D.; Nielsen, L. B.; Jørgensen, S.; Kjaergaard, H. G.; and Wennberg, P. O. Autoxidation of Organic Compounds in the Atmosphere. *J. Phys. Chem. Lett.* **2013**, *4*, 3513-3520.

[62] Orlando, J. J.; Tyndall, G. S. The Atmospheric Chemistry of Alkoxy Radicals. *Chem. Rev.* **2003**, *103*, 4657-4690.

[63] Vereecken, L.; Peeters, J. Decomposition of Substituted Alkoxy Radicals - Part I: A Generalized Structure-Activity Relationship for Reaction Barrier Heights. *Phys. Chem. Chem. Phys.* **2009**, *11*, 9062-9074.

[64] Schrödinger, E. *Statistical Thermodynamics*, Dover Publications, **1989**.

[65] Born, M.; Oppenheimer, R. Zur Quantentheorie der Molekeln. *Annalen der Physik* **1927**, *389*, 457-484.

[66] Hartree, D. R. The Wave Mechanics of an Atom With a Non-Coulomb Central Field. Part I. Theory and Methods. *Proceedings of the Cambridge Philosophical Society* **1928**, *24*, 89.

[67] Hartree, D. R. The Wave Mechanics of an Atom With a Non-Coulomb Central Field. Part II. Some Results and Discussions. *Proceedings of the Cambridge Philosophical Society* **1928**, *24*, 111.

[68] Fock, V. Näherungsmethode zur Lösung des quantenmechanischen mehrkörperproblems. *Zeitschrift fur Physik* **1930**, *61*, 126.

[69] Szabo, A.; Ostlund, N. S. Modern Quantum Chemistry. Introduction to Advanced Electronic Structure Theory. Dover Publications, Inc., Mineola, NY, USA 1996.

[70] Čížek, J. On the Correlation Problem in Atomic and Molecular Systems. Calculation of Wavefunction Components in Ursell-Type Expansion Using Quantum-Field Theoretical Methods. *J. Chem. Phys.* **1966**, *45*, 4256-4266.

[71] Bartlett, R. J. Coupled-Cluster Approach to Molecular Structure and Spectra: A Step Toward Predictive Quantum Chemistry. *J. Phys. Chem.* **1989**, *93*, 1697-1708.

[72] Van Voorhis, T.; Head-Gordon, M. Benchmark Variational Coupled Cluster Doubles Results. J. Chem. Phys. 2000, 113, 8873-8879.

[73] Adler, T. B.; Knizia, G.; Werner, H. A Simple and Efficient CCSD(T)-F12 Approximation. *J. Chem. Phys.* **2007**, *127*, 221106.

[74] Riplinger, C.; Sandhoefer, B.; Hansen, A.; Neese, F. Natural Triple Excitations in Local Coupled Cluster Calculations With Pair Natural Orbitals. J. Chem. Phys. 2013, 139, 134101.

[75] Dirac, P. A. M. Note of Exchange Phenomena in the Thomas Atom. *Cambridge Philos. Soc.* **1930**, *26*, 376-385.

[76] Fermi, E. Eine statistische Methode zur Bestimmung einiger Eigenschaften des Atoms und ihre Anwendung auf die Theorie des periodischen Systems der Elemente. *Z. Phys.* **1928**, *48*, 73-79.

[77] Thomas, L. H. The Calculation of Atomic Fields. *Proc. Cambridge Philos. Soc.* **1927**, *23*, 542-548.

[78] Wigner, E. On the Interaction of Electrons in Metals. *Phys. Rev.* **1934**, *46*, 1002-1011.

[79] Hohenberg, P.; Kohn, W. Inhomogeneous Electron Gas. *Phys. Rev.* **1964**, *136*, 864-871.

[80] Kohn, W.; Sham, L. Self-Consistent Equations Including Exchange and Correlation Effects. *Phys. Rev.* **1965**, *140*, 1133-1138.

[81] Becke, A. D. Density-Functional Exchange-Energy Approximation With Correct Asymptotic Behavior. *Phys. Rev. A* **1988**, *38*, 3098-3100.

[82] Perdew, J. P. Density-Functional Approximation for the Correlation Energy of Inhomogeneous Electron Gas. *Phys. Rev. B* **1986**, *33*, 8822-8824.

[83] Perdew, J. P.; Burke, K.; Ernzerhof, M. Generalized Gradient Approximation Made Simple. *Phys. Rev. Lett.* **1996**, *77*, 3865-3868.

[84] Goerigk, S. L.; Grimme, S. A Thorough Benchmark of Density Functional Methods For General Main Group Thermochemistry, Kinetics, and Non-Covalent Interaction. *Phys. Chem. Chem. Phys.* **2011**, *13*, 6670-6688.

[85] Becke, A. D. Density-Functional Thermochemistry. III. The Role of Exact Exchange. *J. Chem. Phys.* **1993**, *98*, 5648-5652.

[86] Becke, A. D. A New Mixing of Hartree-Fock and Local Density-Functional Theories. *J. Chem. Phys.* **1993**, *98*, 1372-1377.

[87] Grimme, S. Semiemperical Hybrid Density Functional with Perturbative Second-Order Correlation. *J. Chem. Phys.* **2006**, *124*, 034108.

[88] Klimeš, J. Michaelides, A. Perspective: Advances and Challenges in Treating Van Der Waals Dispersion Forces in Density Functional Theory. *J. Chem. Phys.* **2012**, *137*, 120901.

[89] Becke, A. D. Perspective: Fifty Years of Density-Functional Theory in Chemical Physics. *J. Chem. Phys.* **2014**, *140*, 18A301.

[90] Zhao, Y.; Truhlar, D. G. The M06 Suite of Density Functionals for Main Group Thermochemistry, Thermochemical Kinetics, Noncovalent Interactions, Excited States, and Transition Elements: Two New Functionals and Systematic Testing of Four M06-Class Functionals and 12 Other Functionals. *Theor. Chem. Acc.* **2008**, *120*, 215-241.

[91] Grimme, S. Accurate Description of van der Waals Complexes by Density Functional Theory Including Empirical Corrections. *J. Comput. Chem.* **2004**, *25*, 1463-1473.

[92] Grimme, S. Density Functional Theory With London Dispersion Corrections. *Wiley Interdiscip. Rev. Comput. Mol. Sci.* **2011**, *1*, 211-228.

[93] Chai, J. -D.; Head-Gordon, M. Long-Range Corrected Hybrid Density Functionals With Damped Atom-Atom Dispersion Corrections. *Phys. Chem. Chem. Phys.* **2008**, *10*, 6615-6620.

[94] Elm, J.; Bilde, M.; Mikkelsen, K. V. Assessment of Density Functional Theory in Predicting Structures and Free Energies of Reaction of Atmospheric Prenucleation Clusters. *J. Chem. Theor. Comput.* **2012**, *8*, 2071-2077.

[95] Myllys, N.; Elm, J.; Halonen, R.; Kurtén, T.; Vehkamäki, H. Coupled Cluster Evaluation of the Stability of Atmospheric Acid-Base Clusters With up to 10 Molecules. *J. Phys. Chem. A* **2016**, *120*, 621-630.

[96] Myllys, N.; Elm, J.; Kurtén, T. Density Functional Theory Basis Set Convergence of Sulfuric Acid-Containing Molecular Clusters. *Comput. Theor. Chem.* **2016**, *1098*, 1-12.

[97] Brönsted, J. N. Acid and Basic Catalysis. *Chem. Rev.* **1928**, *5*, 231-338.

[98] Bell, R. P. The Theory of Reactions Involving Proton Transfers. *Proc. R. Soc. London, Ser. A* **1936**, *154*, 414-429.

[99] Evans, M. G.; Polanyi, M. Inertia and Driving Force of Chemical Reactions. *Trans. Faraday Soc.* **1938**, *34*, 11-24.

[100] Thomson, J. J. On the Appearance of Helium and Neon in Vacuum Tubes. *Nature* **1913**, *90*, 645-647.

[101] Aston, F. W. A Positive Ray Spectrograph. *Philos. Mag.* **1919**, *38*, 707.

[102] Prather, K. A.; Nordmeyer, T.; Salt, K. Real-time Characterization of Individual Aerosol Particles Using Time-Of-Flight Mass Spectrometry. *Anal. Chem.* **1994**, *66*, 1403-1407.

[103] Henderson, W.; McIndoe, J. S. Mass Spectrometry of Inorganic and Organometallic Compounds. *John Wiley and Sons*: *Chichester* **2005**.

[104] Banoub, J. H.; Newton, R. P.; Esmans, E.; Ewing, D. F.; Mackenzie, G. Recent Developments in Mass Spectrometry For Characterization of Nucleosides, Nucleotides, Oligonucleotides, and Nucleic Acids. *Chem. Rev.* **2005**, *105*, 1869-1915.

[105] Steiger, R. v.; Schwadron, N. A.; Fisk, L. A.; Geiss, J.; Gloeckler, G.; Hefti, S.; Wilken, B.; Wimmer-Schweingruber, R. F.; Zurbuchen, T. H. Composition of Quasi-Stationary Solar Wind Flows from Ulysses/Solar Wind Ion Composition Spectrometer. *J. Geo. Phys. Res.* **2000**, *105*, 27217-27238.

[106] Waite Jr., J. H.; Niemann, H.; Yelle, R. V.; Kasprzak, W. T.; Cravens, T. E.; Luhmann, J. G.; McNutt, R. L.; Ip, W.- H.; Gell, D.; Haye, V. D. L.; et al. Ion Neutral Mass Spectrometer Results from the First Flyby of Titan. *Science* **2005**, *308*, 982-986.

[107] Lewis, R. J.; Jones, A.; Vernoux, J.- P. HPLC/Tandem Electrospray Mass Spectrometry for the Determination of Sub-ppb Levels of Pacific and Caribbean Ciguatoxins in Crude Extracts of Fish. *Anal. Chem.* **1999**, *71*, 247-250.

[108] Harvey, D. J. Identification of Protein-Bound Carbohydrates by Mass Spectrometry. *Proteomics* **2001**, *1*, 311-328.

[109] Nordhoff, E.; Kirpekar, F.; Roepstorff, P. Mass Spectrometry of Nucleic Acids. *Mass Spec. Rev.* **1996**, *15*, 67-138.

[110] Dagan, S.; Amirav, A. Electron Impact Mass Spectrometry of Alkanes in Supersonic Molecular Beams. *J. Am. Soc. Mass Spectrom.* **1995**, *6*, 120-131.

[111] Junninen, H.; Ehn, M.; Petäjä, T.; Luosujärvi, L.; Kotiaho, T.; Kostiainen, R.; Rohner, U.; Gonin, M.; Fuhrer, K.; Kulmala, M.; Worsnop, D. R. A High-Resolution Mass Spectrometer to Measure Atmospheric Ion Composition. *Atmos. Meas. Tech.* **2010**, *3*, 1039-1053.

[112] Merchant, M.; Weinberger, S. R. Recent Advancements in Surface-Enhanced Laser Desorption/Ionization-Time of Flight-Mass Spectrometry. *Electrophoresis* **2000**, *21*, 1164-1167.

[113] Kürten, A.; Bergen, A.; Heinritzi, M.; Leiminger, M.; Lorenz, V.; Piel, F.; Simon, M.; Sitals, R.; Wagner, A. C.; Curtius, J. Observation of New Particle Formation and Measurement of Sulfuric Acid, Ammonia, Amines and Highly Oxidized Organic Molecules at a Rural Site in Central Germany. *Atmos. Chem. Phys.* **2016**, *16*, 12793-12813.

[114] Zhao, J.; Smith, J. N.; Eisele, F. L.; Chen, M.; Kuang, C.; McMurry, P. H.: Observation of Neutral Sulfuric Acid-Amine Containing Clusters in Laboratory and Ambient Measurements. *Atmos. Chem. Phys.* **2011**, *11*, 10823-10836.

[115] Jokinen, T.; Sipilä, M.; Junninen, H.; Ehn, M.; Lönn, G.; Hakala, J.; Petäjä, T.; Mauldin III, R. L.; Kulmala, M.; Worsnop, D. R. Atmospheric Sulphuric Acid and Neutral Cluster Measurements Using CI-APi-TOF. *Atmos. Chem. Phys.* **2012**, *12*, 4117-4125.

[116] Sarnela, N.; Jokinen, T.; Nieminen, T.; Lehtipalo, K.; Junninen, H.; Kangasluoma, J.; Hakala, J.; Taipale, R.; Schobesberger, S.; Sipilä, M.; Larnimaa, K.; Westerholm, H.; Heijari, J.; Kerminen, V.-M.; Petäjä, T.; Kulmala, M. Sulphuric Acid and Aerosol Particle Production in the Vicinity of an Oil Refinery. *Atmos. Environ.* **2015**, *119*, 156-166.

[117] Tröstl, J.; Chuang, W. K.; Gordon, H.; Heinritzi, M.; Yan, C.; Molteni, U.; Ahlm, L.; Frege, C.; Bianchi, F.; Wagner, R.; et al. The Role of Low-Volatility Organic Compounds in Initial Particle Growth in the Atmosphere. *Nature* **2016**, *533*, 527-531.

[118] Mentel, T. F.; Springer, M.; Ehn, M.; Kleist, E.; Pullinen, I.; Kurtén, T.; Rissanen, M.; Wahner, A.; Wildt, J. Formation of Highly Oxidized Multifunctional Compounds: Autoxidation of Peroxy Radicals Formed in the Ozonolysis of Alkenes - Deduced from Structure-Product Relationships. *Atmos. Chem. Phys.* **2015**, *15*, 6745-6765.

[119] Hyttinen, N.; Kupiainen-Määttä, O.; Rissanen, M. P.; Muuronen, M.; Ehn, M.; Kurtén, T. Modeling the Charging of Highly Oxidized Cyclohexene Ozonolysis Products Using Nitrate-Based Chemical Ionization. *J. Phys. Chem. A* **2015**, *119*, 6339-6345.

[120] Hyttinen, N.; Otkjær, R. V.; Iyer, S.; Kjaergaard, H. G.; Rissanen, M. P.; Wennberg, P. O.; Kurtén, T. Computational Comparison of Different Reagent Ions in the Chemical Ionization of Oxidized Multifunctional Compounds. *J. Phys. Chem. A* **2018**, *122*, 269-279.

[121] Berndt, T.; Richters, S.; Kaethner, R.; Voigtländer, J.; Stratmann, F.; Sipilä, M.; Kulmala, M.; Herrmann, H. Gas-Phase Ozonolysis of Cycloalkenes: Formation of Highly Oxidized RO_2 Radicals and Their Reactions with NO, NO_2, SO_2, and Other RO_2 Radicals. *J. Phys. Chem. A* **2015**, *119*, 10336-10348.

[122] Berndt, T.; Richters, S.; Jokinen, T.; Hyttinen, N.; Kurtén, T.; Otkjær, R. V.; Kjaergaard, H. G.; Stratmann, F.; Herrmann, H.; Sipilä, M.; et al. Hydroxyl Radical-Induced Formation of Highly Oxidized Organic Compounds. *Nat. Commun.* **2016**, *7*, 13677.

[123] Richters, S.; Herrmann, H.; Berndt, T. Different Pathways of the Formation of Highly Oxidized Multifunctional Organic Compounds (HOMs) from the Gas-Phase Ozonolysis of β-Caryophyllene. *Atmos. Chem. Phys.* **2016**, *16*, 9831-9845

[124] Richters, S.; Herrmann, H.; Berndt, T. Highly Oxidized RO_2 Radicals and Consecutive Products from the Ozonolysis of Three Sesquiterpenes. *Environ. Sci. Technol.* **2016**, *50*, 2354-2362.

[125] Hyttinen, N.; Rissanen, M. P.; Kurtén, T. Computational Comparison of Acetate and Nitrate Chemical Ionization of Highly Oxidized Cyclohexene Ozonolysis Intermediates and Products. *J. Phys. Chem. A* **2017**, *121*, 2172-2179.

[126] Chhabra, P. S.; Lambe, A. T.; Canagaratna, M. R.; Stark, H.; Jayne, J. T.; Onasch, T. B.; Davidovits, P.; Kimmel, J. R.; Worsnop, D. R. Application of High-Resolution Time-of-Flight Chemical Ionization Mass Spectrometry Measurements to Estimate Volatility Distributions of α-Pinene and Naphthalene Oxidation Products. *Atmos. Meas. Tech.* **2015**, *8*, 1-18.

[127] Yatavelli, R. L. N.; Lopez-Hilfiker, F.; Wargo, J. D.; Kimmel, J. R.; Cubison, M. J.; Bertram, T. H.; Jimenez, J. L.; Gonin, M.; Worsnop, D. R.; Thornton, J. A. A Chemical Ionization High-Resolution Time-of-Flight Mass Spectrometer Coupled to a Micro Orifice Volatilization Impactor (MOVI-HRToF-CIMS) for Analysis of Gas and Particle-Phase Organic Species. *Aerosol Sci. Technol.* **2012**, *46*, 1313-1327.

[128] Veres, P.; Roberts, J. M.; Warneke, C.; Welsh-Bon, D.; Zahniser, M.; Herndon, S.; Fall, R.; de Gouw, J. Development of Negative-Ion Proton-Transfer Chemical-Ionization Mass Spectrometry (NI-PTCIMS) for the Measurement of Gas-Phase Organic Acids in the Atmosphere. *Int. J. Mass Spectrom.* **2008**, *274*, 48-55.

[129] Bertram, T. H.; Kimmel, J. R.; Crisp, T. A.; Ryder, O. S.; Yatavelli, R. L. N.; Thornton, J. A.; Cubison, M. J.; Gonin, M.; Worsnop, D. R. A Field-Deployable, Chemical Ionization Time-of-Flight Mass Spectrometer. *Atmos. Meas. Tech.* **2011**, *4*, 1471-1479.

[130] Iyer, S.; Lopez-Hilfiker, F.; Lee, B. H.; Thornton, J. P.; Kurtén, T. Modeling the Detection of Organic and Inorganic Compounds Using Iodide-Based Chemical Ionization. *J. Phys. Chem. A* **2016**, *120*, 576-587.

[131] McNeill, V. F.; Wolfe, G. M.; Thornton, J. A. The Oxidation of Oleate in Submicron Aqueous Salt Aerosols: Evidence of a Surface Process. *J. Phys. Chem. A* **2007**, *111*, 1073-1083.

[132] Caldwell, G.; Renneboog, R.; Kebarle, P. Gas-phase acidities of aliphatic carboxylic-acids, based on measurements of proton-transfer equilibria. *Can. J. Chem.* **1989**, *67*, 611-618.

[133] Lee, B. H.; Lopez-Hilfiker, F. D.; Mohr, C.; Kurten, T.; Worsnop, D. R.; Thornton, J. An Iodide-Adduct High-Resolution Time-of-Flight Chemical-Ionization Mass Spectrometer: Application to Atmospheric Organic and Inorganic Compounds. *Environ. Sci. Technol.* **2014**, *48*, 6309-6317.

[134] Sanchez, J.; Tanner, D. J.; Chen, D.; Huey, L. G.; Ng, H. L. A New Technique for the Direct Detection of HO_2 Radicals using Bromide Chemical Ionization Mass Spectrometry (Br-CIMS): Initial Characterization. *Atmos. Meas. Tech.* **2016**, *9*, 3851-3861.

[135] Albrecht, S. R.; Novelli, A.; Hofzumahaus, A.; Kang, S.; Baker, Y.; Mentel, T.; Wahner, A.; Fuchs, H. Measurement of Hydroperoxy Radicals (HO_2) at Atmospheric Concentrations using Bromide Chemical Ionisation Mass Spectrometry. *Atmos. Meas. Tech.* **2019**, *12*, 891-902.

[136] Su, T.; Bowers, M. T. Theory of Ion-Polar Molecule Collisions. Comparison With Experimental Charge Transfer Reactions of Rare Gas Ions to Geometric Isomers of Diurobenzene and Dichloroethylene. *J. Chem. Phys.* **1973**, *58*, 3027.

[137] Passananti, M.; Zapadinsky, E.; Zanca, T.; Kangasluoma, J.; Myllys, N.; Rissanen, M. P.; Kurtén, T.; Ehn, M.; Attoui, M.; Vehkamäki, H. How Well Can We Predict Cluster Fragmentation Inside a Mass Spectrometer? *Chem. Commun.* **2019**, *55*, 5946-5949.

[138] Albrecht, S. R.; Novelli, A.; Hofzumahaus, A.; Kang, S.; Baker, Y.; Mentel, T.; Wahner, A.; Fuchs, H. Measurements of Hydroperoxy Radicals (HO_2) at Atmospheric Concentration Using Bromide Chemical Ionization Mass Spectrometry. *Atmos. Meas. Tech.* **2019**, *12*, 891-902.

[139] Zapadinsky, E.; Passananti, M.; Myllys, N.; Kurtén, T.; Vehkamäki, H. Modeling on Fragmentation of Clusters inside Mass Spectrometer. *J. Phys. Chem. A* **2019**, *123*, 611-624.